Biophysical modeling of actin-mediated structural plasticity reveals mechanical adaptation in dendritic spines

M. Bonilla-Quintana, P. Rangamani**

Department of Mechanical and Aerospace Engineering, University of California San Diego, La Jolla CA 92093, USA.

**To whom correspondence must be addressed: prangamani@ucsd.edu

Abstract

Synaptic plasticity is important for learning and memory formation and describes the strengthening or weakening of connections between synapses. The postsynaptic part of excitatory synapses resides in dendritic spines, which are small protrusions from the dendrites. One of the key features of synaptic plasticity is that it is correlated with the size of these spines. A long-lasting synaptic strength increase (long-term potentiation, LTP) is only possible through the reconfiguration of the actin spine cytoskeleton. Here, we developed an experimentally-informed three-dimensional computational model in a moving boundary framework, which describes the reactions between actin, and actin-binding proteins (ABPs) leading to the cytoskeleton reconfiguration, and their effect in the spine membrane shape, to examine the spine enlargement upon LTP. Our model predicts that spine enlargement during LTP is viscoelastic in nature. We found that volume increase in the spine was more efficient if the stimulus-triggered influx of actin and ABPs were spatially compartmentalized. In response to repeated stimuli, our model predicts that spine growth can be self-regulated by tuning the viscoelastic properties. Thus, we conclude that variation of the viscoelastic properties under different conditions hints at a mechanical regulation of spine expansion during LTP.

Keywords:

Dendritic spines, sLTP, actin, 3D model, PDEs, moving boundaries, viscoelastic materials.

1 Significance Statement

Dendritic spines are small bulbous protrusions that receive stimulation from presynaptic neurons. Upon stimulation, the dendritic spines change their size, a feature which is hindered during disease. The change in spine size during stimulation is achieved by changes to the actin cytoskeleton and mediated by many actin-binding proteins. To investigate the fundamental mechanics of spine expansion, we developed a minimal 3D model that accounts for the dynamics of cytoskeleton-membrane interactions involved in spine shape changes. Our simulations predict that spine expansion due to actin remodeling can be captured using simple viscoelastic relationships. Additionally, we also found that these mechanical properties can change under different stimuli, allowing for mechanical tuning of spine growth. Thus, we find that spine growth is regulated by the mechanical properties of the spine.

2 Introduction

Dendritic spines are small protrusions from dendrites that form the postsynaptic part of a vast majority of excitatory synapses (*1–3*). In response to glutamate signals released by stimulated presynaptic neurons, spines undergo both biochemical and morphological changes that can be

long-lasting (*4–6*) (Fig. 1). Such changes have been long hypothesized as the biological mechanisms underlying memory storage in the brain (*7*). One of the most studied long-lasting changes in dendritic spines is long-term potentiation (LTP). It is characterized by an enhancement in strength and duration of the postsynaptic response to an electrical stimulus in the presynaptic terminal that causes a large release of glutamate (*8*). The α-amino-3-hydroxy-5-methyl-4-isoxazolepropionic acid receptors (AMPARs) located at the postsynaptic density (PSD), a dense receptor site at the tip of the spine, take up the released glutamate from the presynaptic terminal. A high concentration of glutamate depolarizes the spine membrane, which causes the release of the magnesium (Mg^{2+}) block on the N-methyl-D-aspartate receptors (NMDARs) and allows the entry of calcium (Ca^{2+}) into the spine (*9*). The activation of the NMDARs induces an increase in the number of AMPARs in the PSD (*10*), enhancing the uptake of glutamate and thus strengthening the spine response.

The volume of dendritic spines correlates with the PSD area (*11*) and the spine structure is affected by LTP induction. It has been shown that spines increase their volume dramatically, up to 390%, after stimulation (*12*, *13*). Such a volume increase is associated with an increase in AMPAR-mediated currents and depends on NMDAR activation and actin polymerization (*4*). Actin is highly concentrated in dendritic spines (*14*) and plays a key role in LTP (*3*, *15*). Crucially, actin remodeling is critical for spine enlargement. Recent experiments have shown that F-actin in the spine is divided into different pools: the dynamic pool and the stable pool (*16*). In contrast to the stable pool of actin, with a lifetime of $\sim$17 min, the dynamic pool undergoes rapid treadmilling ($\sim$40 s), generating an expansive force caused by actin polymerization (*16*). Moreover, the equilibrium between G-actin and F-actin is affected by stimulation (*5*), suggesting that structural reconfiguration of actin is necessary for spine enlargement. The term structural LTP (sLTP) is used to refer to the long-term enlargement of dendritic spines (*2*, *17*).

Actin binding proteins (ABPs) aid the reconfiguration of the cytoskeleton by promoting G-actin polymerization, F-actin depolymerization, and capping the F-actin ends, which prevents their polymerization and depolymerization (*18*). Experiments have shown that ABPs are necessary for LTP (*15*, *19*). For example, conditional mutagenesis of Arp2/3, which promotes actin branching (*18*, *20*), hinders spine enlargement upon LTP and is implicated in psychiatric disorders (*21*). Loss of cofilin impairs learning (*22*). Cofilin is an ABP whose function depends on its relative concentration with actin; it either severs F-actin at low concentration or promotes actin nucleation at high concentration (*23*). To achieve the transient size increase seen during the first 4-7 minutes of LTP (*12*, *13*), in addition to the Arp2/3 and cofilin activation due to Ca^{2+} influx (*24*) (Fig. 1C), translocation of ABPs into the spine is necessary (*25*). Although this translocation process is not fully understood, it has been hypothesized that spines become “tagged” for protein capture during the early phase of LTP (*26*, *27*). Experiments inducing sLTP by glutamate uncaging for 1 minute have identified different groups of proteins according to the change of their concentrations over time. These groups are divided depending on whether proteins show 1) a persistent increase, 2) a transient increase, 3) a transient decrease, or 4) a persistent decrease in their concentration (*25*). After three hours, the spine settles to a size that is 40% larger than that before LTP induction (*12*, *13*). Hence, the reconfiguration of the actin cytoskeleton of dendritic spines; and thus, structural plasticity is possible by an orchestrated interplay between actin and ABPs triggered by different signaling pathways (*25*). Spine mechanical properties, such as elastic storage modulus and viscous loss modulus increase upon LTP, which facilitate mechanical stabilization due to spine stiffening of the internal structure (*28*). Furthermore, recent experimental data shows that actin polymerization alone is insufficient for spine expansion and that mechanical coupling of the actin filaments with the extracellular environment through clutch molecules is necessary to push the membrane forward (*29*). Therefore, both biochemical reactions and mechanical forces are paramount to sLTP.

In this work, we seek to answer the following questions: Can a minimal model of actin-membrane interactions capture the dynamics of spine changes during sLTP? How do different fluxes of ABPs affect spine dynamics during sLTP? How do membrane properties and interactions with clutch molecules, which couple the actin network to the extracellular matrix, affect sLTP? And finally, how do multiple stimuli affect sLTP? To answer these questions, we develop a 3D computational model using a system of partial differential equations with moving boundaries to incorporate the spatio-temporal dynamics of actin and ABPs in the expanding dendritic spines. In the following work, we describe the governing equations and the computational implementation, and systematically investigate the contribution of ABPs and mechanics to sLTP under different stimuli. Our results show that actin elongation, branching, severing, and capping are sufficient to capture the dynamics of spine growth during sLTP and predict that the spine acts as a viscoelastic object. Moreover, the mechanics of the spine also enhances the spine response to sLTP through the coupling of the actin filaments with the extracellular environment. These results are discussed in detail below.

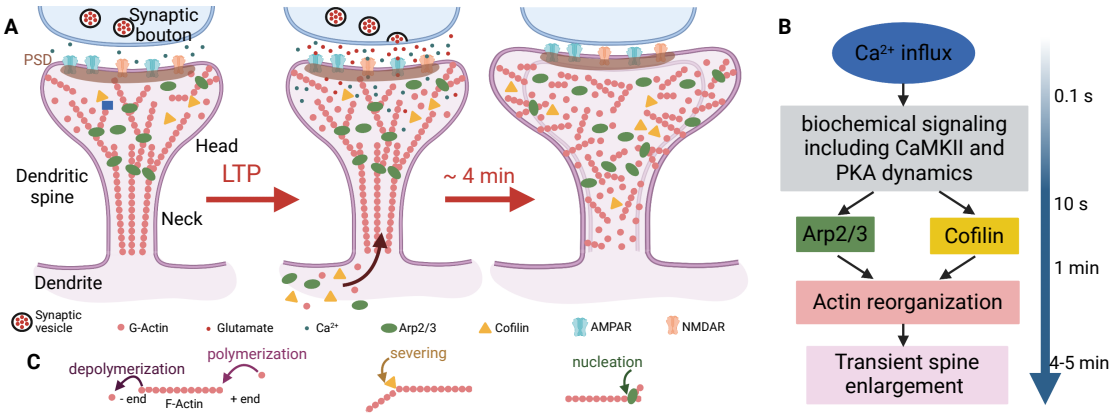

Figure 1: Biophysical events involving early structural plasticity in the dendritic spine. **A)** Upon LTP induction, glutamate is released from the presynaptic neuron and taken up by the postsynaptic neuron. Consequently, a cascade of chemical reactions is initiated **(B)**, and an influx of actin, cofilin, and Arp2/3 into the spine is triggered. This remodels the spine cytoskeleton allowing for spine enlargement. **C)** Actin filament treadmilling, branching, and severing events, which remodel the cytoskeleton. In this model, we focus on how the spatio-temporal dynamics of actin, cofilin, and Arp2/3 dictate the shape of the dendritic spine. Image created with `BioRender.com`

3 Model development

We develop a mathematical model in which F-actin dynamics in the dendritic spine are affected by Arp2/3 and cofilin. As in cell motility models (*30–32*), we assume that these ABPs are sufficient to promote membrane protrusion because the force generated by actin polymerization overcomes the membrane resistance (*33*, *34*). In the model, actin, Arp2/3, and cofilin are free to diffuse in the spine volume. Upon LTP, there is an influx of these proteins into the spine that represents the translocation of ABPs.

3.1 Governing equations

Based on the assumptions described above, we formulate a system of partial differential equations that describe the spatio-temporal dynamics of F-actin barbed ends, Arp2/3, and cofilin. This system is coupled with the spine membrane dynamics, as described in (*35*), enabling us to investigate the influence of ABPs in spine size and shape changes over time.

3.1.1 Actin dynamics

F-actin in dendritic spines is distributed in two different pools, the stable pool and the dynamic pool. We assume that the structural changes in dendritic spines are mostly driven by the dynamic pool that has short filaments with uncapped (+) ends (or barbed ends). Therefore, we do not explicitly model the stable pool, which only accounts for 5% of the total F-actin (*16*). F-actin (+) ends are continuously polymerizing at a velocity, ν. Since the dynamic pool treadmills fast and accounts for the 95% of F-actin in the spine (*16*), we take the actin polymerization velocity to be fixed and independent of actin concentration. Moreover, we assume that actin and ATP are not depleted throughout the simulation. The polymerization of F-actin near the dendritic spine membrane generates a force that pushes the membrane forward (*34*, *36*). Therefore, we keep track of the number of barbed ends per unit volume $B(\mathbf{r},t)$ at position $\mathbf{r} \in \mathcal{L} \subset \mathbb{R}^3$, where $\mathcal{L}$ is a cubic lattice domain (see Fig. S7), instead of F-actin or G-actin concentration.

The dynamics of the barbed ends are given by

$$\begin{aligned}\frac{\partial B}{\partial t} = & \underbrace{\rho}_{\text{motion of barbed ends}} - \underbrace{k_\beta B}_{\text{basal efflux}} \\ & + \underbrace{\Psi_0}_{\text{scale factor}} \left(\underbrace{f_{nuc}}_{\text{nucleation function}} + \underbrace{f_{sev}}_{\text{severing function}} + \underbrace{I_\beta}_{\text{basal influx}} + \underbrace{I_{S,\beta}(\mathbf{r},t)}_{\text{stimulus-triggered influx}} \right),\end{aligned} \tag{1}$$

where k_β is a constant basal efflux rate. The basal influx I_β of actin is due to local actin synthesis in the dendrite (*37*, *38*). The stimulus-triggered influx $I_{S,\beta}$ mimics the transient influx upon stimulation (*25*). Hence, it is nonzero only during a brief window of time after stimulus initiation (1 minute). Because the proteins used in the model are dispersed in the spine, we assume a homogeneous basal influx. In line with experimental observations (*25*), we localize the stimulus-triggered influx to the spine head. For consistency of units, these terms are multiplied by a conversion factor Ψ_0 that changes from concentration units in μM to the number of barbed ends per μm^3. We assume that F-actin polymerization takes place shortly after actin enters the spine. Note that ρ provides the only spatial dependence in Eq. (1), because we assume the diffusivity and the free flow of barbed ends to be minimal.

The motion of the barbed ends toward the cell membrane is given by

$$\rho = \left(\underbrace{\eta \nabla \cdot \mathbf{f}_u}_{\text{F-actin retrograde flow}} - \underbrace{\nabla \cdot \nu \mathbf{d}}_{\text{F-actin elongation}} \right) B, \tag{2}$$

where ∇ is the gradient operator. Here, the filament elongates in the direction $\mathbf{d} = \nabla \mathrm{d}(\mathbf{r},\Gamma)$ by polymerization of G-actin, where d is the shortest distance from a location $\mathbf{r} \in \mathcal{L}$ to the membrane $\Gamma = \partial\Omega$. The membrane encloses the spine in the evolving domain $\Omega = \Omega(t)$ (see Fig. S9). Thus, F-actin in the dynamic pool grows towards the closest direction to the membrane at a free polymerization velocity ν. When barbed ends are close to the membrane, polymerization of G-actin induces a backward F-actin flow to fit a G-actin between the membrane and the barbed end. This backward flow is called F-actin retrograde flow. In Eq. (2),

$$\mathbf{f}_u = -\frac{\partial \psi}{\partial \mathbf{r}}, \tag{3}$$

is a force density that confines the system to Ω, as in (*35*). It is determined from the soft repulsive potential

$$\psi = \psi(\mathbf{r},\Gamma) = \alpha \tanh\left(\beta \mathrm{sign}(\mathbf{r}) \mathrm{d}(\mathbf{r},\Gamma)\right)/2, \tag{4}$$

where $\mathrm{sign}(\mathbf{r})$ represents the sign function that is negative for $\mathbf{r} \in \Omega$ and positive otherwise. If $\alpha, \beta \longrightarrow \infty$, the membrane is a reflective boundary. In the F-actin retrograde flow, η represents the interaction with other cellular elements and can be interpreted as a drag term. Thus, the spatial motion of the barbed ends is dominated by ρ, which can be interpreted as a drift of F-actin towards the membrane.

The nucleation function accounts for the nucleation of new filaments with uncapped (+) ends by Arp2/3 binding to actin filaments. We choose the nucleation function proposed by (*39*)

$$f_{nuc} = f_{nuc}(A, B) = k_{nuc} A \Psi_1 B, \tag{5}$$

which reflects the side-branching of Arp2/3. This function agrees with the observations in (*40*), where the nucleation of new filaments is enhanced on the side of bend filaments. Here, k_{nuc} represents the nucleation rate, A is the Arp2/3 concentration, and Ψ_1 is a unit conversion factor.

Cofilin severs F-actin in a concentration-dependent manner (*23*), creating new filaments with uncapped (+) ends. Based on observations of (*25*), we assume that during the first few minutes after LTP the concentration of F-actin in the spine is higher than the concentration of cofilin. Because cofilin severs F-actin at low concentrations (*23*), we assume that cofilin binding to F-actin is cooperative (*41*). This is represented by the severing rate function

$$f_{sev} = f_{sev}(C, B) = k_{sev} \frac{C^n}{k_n + C^n} \Psi_1 B, \tag{6}$$

where k_{sev} is the severing rate, k_n is the dissociation constant, n is the Hill coefficient, and C represents the concentration of cofilin.

3.1.2 Arp2/3 Dynamics

The evolution of Arp2/3 concentration over time is given by

$$\frac{\partial A}{\partial t} = \underbrace{\xi \rho \Psi_1 A}_{\text{bulk flow}} - \underbrace{k_A A}_{\text{degradation}} - \underbrace{f_{nuc}}_{\text{nucleation function}} + \underbrace{I_A}_{\text{basal influx}} + \underbrace{I_{S,A}(\mathbf{r}, t)}_{\text{stimulus-triggered influx}}, \tag{7}$$

where k_A is a constant degradation rate. We assume that as the dendritic spine expands, the Arp2/3 molecules are transported towards the membrane by a bulk flow, as in (*32*). The velocity of the bulk flow is given by $\xi\rho$, $0 < \xi < 1$. Note that this velocity is slower than the motion of barbed ends to account for cytoplasmic viscosity.

3.1.3 Cofilin Dynamics

The evolution of cofilin concentration is given by

$$\frac{\partial C}{\partial t} = \underbrace{\xi \rho \Psi_1 C}_{\text{bulk flow}} - \underbrace{k_C C}_{\text{degradation}} - \underbrace{f_{sev}}_{\text{severing function}} + \underbrace{I_C}_{\text{basal influx}} + \underbrace{I_{S,C}(\mathbf{r}, t)}_{\text{stimulus-triggered influx}}, \tag{8}$$

where k_C is the degradation rate. Note that cofilin is also transported by bulk flow towards the membrane at velocity $\xi\rho$.

3.1.4 Membrane Dynamics

The membrane Γ evolves according to

$$\frac{\mathrm{d}\Gamma}{\mathrm{d}t} = \zeta \left(\mathbf{F}_{mem} + \mathbf{F}_{actin} \right), \tag{9}$$

where ζ is a drag coefficient. The force generated by the polymerization of uncapped barbed ends B is given by

$$\mathbf{F}_{actin} = -\frac{\partial \mathcal{E}_B}{\partial \Gamma}. \tag{10}$$

Following (*35*), the force applied to the membrane by these filaments is given by

$$\mathcal{E}_B = \int_{\Omega} \mathrm{d}\mathbf{r} \psi(\mathbf{r}, \Gamma) B(\mathbf{r}). \tag{11}$$

The force generated by actin is balanced by a force generated by the membrane $\mathbf{F}_{mem}$, which counteracts membrane deformations and is given by

$$\mathbf{F}_{mem} = -\frac{\partial \mathcal{E}_{mem}}{\partial \Gamma}, \tag{12}$$

where

$$\mathcal{E}_{mem} = \frac{\kappa}{2} \int_{\Gamma} \mathrm{d}A H^2 \tag{13}$$

represents the membrane Helfrich free energy due to bending (*42*). Here, H is the mean curvature, and κ is the bending modulus. Note that we consider the membrane as a 2D elastic continuum with negligible thickness, as in (*43*, *44*). The volume and surface area of the spine membrane are unconstrained due to the influx of proteins and membrane addition through trafficking mechanisms (*17*). Thus, in our model, the membrane tension and the osmotic pressure are ignored because the surface area and the volume are not constrained.

3.2 Numerical implementation

In the model, the dynamics of actin barbed ends, Arp2/3, and cofilin are given by Eqs. (1),(7), and (8). In the simulation, these equations are solved over time in a cubic domain with an embedded triangular mesh representing the dendritic spine membrane (Fig. S12A). A signed distance function is used to calculate the proximity of the chemical species to the membrane (Fig. S12B). The force generated by actin polymerization and the force generated by the membrane are calculated from the spatial location of the barbed ends and the geometry of the spine mesh, respectively. These forces dictate the evolution of the spine mesh (Eq. 9). To reach a stable spine morphology, we set the basal influx to be homogeneously distributed inside the spine. This basal influx remains in the same location throughout the simulation (cyan circles in Fig. 2A). We assume that the stimulus-triggered influx rapidly reaches the spine head at Δ_x distance from the membrane and within $z = 0.6$ and $z = 1$ µm (red triangles in Fig. 2A). We delimit the height of the stimulus location to capture the observations that the PSD configuration remains stable during the early phase of sLTP (*12*, *25*), *i.e.*, the duration of the simulations. Finally, we scale the stimulus-triggered influx to the initial head size to ensure that the same amount of proteins flows into the spine during the stimulus time window.

We solve the system of partial differential equations using MATLAB's (*45*) `ode45` solver at each time-step Δ_t for all positions $\mathbf{r}$ of a discretized cubic lattice domain $\mathcal{L} \in \mathbb{R}^3$ with Δ_x spacing

(Fig. S7D). The Laplace and gradient operators are discretized using an explicit finite differences scheme. The spine membrane Γ is approximated by a 3D polygon with a triangular isotropic mesh consisting of n_v vertices located at $\mathbf{s}_i \in \mathbb{R}^3, i \in \{1, 2, \ldots, n_v\}$ (Fig. S7E). Γ is updated according to Eq.(9) at each time-step. For numerical accuracy, the membrane is remeshed using an isotropic remesher (*46*) (based on `OpenMesh` (*47*)), with a target edge length of Δ_s. The points corresponding to the dendritic base are fixed throughout the simulation (Fig. S12A). See Figure S8 for a flowchart of the simulation.

3.3 Constraining kinetic parameters to experimental measurements.

Experimental results from (*25*) are the foundations for the temporal dynamics of the number of barbed ends, and Arp2/3 and cofilin concentration in our model. Therefore, we fit the model parameters to the data in (*25*) that shows the normalized concentrations of actin, Arp2/3, and cofilin in dendritic spines of hippocampal CA1 neurons after inducing sLTP by 2P glutamate uncaging for 1 minute (Fig. S11A-B, see Supplementary Information S2.2 for details). Briefly, we use a nonlinear least square solver to fit the parameters (I, I_S, and k) to the experimental concentration traces of actin, Arp2/3, and cofilin. The goodness of the fit was assessed by the squared norm of the residual. Supplementary Information S2 contains further details of parameter fitting. Other parameters are taken from the literature or set to a physiological range (Table 1).

To capture the mechanical properties of the spine, we fit a Kelvin-Voigt viscoelastic model, using similar tools as with the experimental data described above (see Supplementary Information S2.3 for details). We use the normalized volume over time as a proxy for the change in length over time. We assume that during the stimulation window, the spine is subject to constant stress.

3.4 Stimulus

In our model, the stimulus from the presynaptic terminal triggers an influx of proteins into the spine, consistent with the observations in (*25*). Therefore, we assume that the stimulus-triggered terms $I_{S,\beta}$, $I_{S,A}$, and $I_{S,C}$ in Eqs. (1), (7), and (8), respectively, are set to the values in Table 1 during the 1 minute period, and zero otherwise. Before and after the stimulus window, these terms are equal to zero. This stimulus-triggered influx is normalized for the spine volume, so the amount of stimulus-triggered influx is independent of the size of the spine.

Table 1: Model Parameters For further information about parameter fitting see Supplementary Information S2.

Symbol	Definition	Units	Value	Reference
k_β	actin degradation rate	1/s	0.0081	fitted to (*25*)
I_β	actin basal influx	μM/s	24.4284	fitted to (*25*)
$I_{S,\beta}$	actin stimulus influx	μM/s	25.6684	fitted to (*25*)
k_A	Arp2/3 degradation rate	1/s	0.0013	fitted to (*25*)
I_A	Arp2/3 basal influx	μM/s	0.0255	fitted to (*25*)
$I_{S,A}$	Arp2/3 stimulus influx	μM/s	0.0293	fitted to (*25*)
k_C	cofilin degradation rate	1/s	0.0006	fitted to (*25*)
I_C	cofilin basal influx	μM/s	0.0237	fitted to (*25*)
$I_{S,C}$	cofilin stimulus influx	μM/s	0.4384	fitted to (*25*)
k_{nuc}	nucleation rate	1/(μM s)	0.0153	(*39*)
k_{sev}	cofilin severing rate	1/s	0.0120	(*48*)
n	Hill coefficient for cofilin binding	-	3.5	(*41*)
k_n	dissociation constant	μM^n	0.6	(*41*)
Ψ_0	scale factor converting to number of barbed ends per μm^3	$\#/(\mu m^3 \mu M)$	3.6	fitted
Ψ_1	scale factor converting to concentration	μm^{3}μM/#	0.02	fitted
ν	F-actin polymerization velocity	μm/s	0.05	(*49*)
ξ	conversion constant	1/μM	0.05	fitted
α	amplitude of the repulsive potential	pN	65	fitted
β	steepness of the repulsive potential	-	40	fitted
η	effective filament mobility	μm/(pN s)	0.00005	fitted
ζ	strength of force update (inverse of drag coefficient)	μm/(s pN)	0.001	fitted
κ	bending modulus	pN μm	0.18	(*50*)
Δ_t	time-step	s	0.01	fitted
Δ_x	cubic lattice interval length	μm	0.0315	fitted
Δ_s	edge length	μm	0.05	fitted

4 Results

Using a minimal model for spine actin-membrane interactions, we investigated the temporal and spatial evolution of the number of barbed ends and concentration of Arp2/3 and cofilin. Our simulations were able to qualitatively capture the experimental observations of spine growth during sLTP. Further analysis revealed that the spine acts as a viscoelastic object during sLTP; the spring and dashpot constants are tuned by the biophysical effects of actin-membrane-clutch protein interactions under different stimuli. This ability to tune the viscoelastic properties of the spine may be underlying the ability of spines to find the balance between growth and stabilization. These results are discussed in detail below.

4.1 Spine enlargement during LTP is viscoelastic in nature

We first investigated the spatial interaction of the ABPs (Arp2/3 and cofilin) with actin in our model. Having established the mechanical equilibrium (see Supplementary Information S4), we simulated sLTP induction in the spines by activating the stimulus-triggered influx inside the head (Fig. 2A) for 1 minute (i.e., setting $I_{S,\beta}, I_{S,A}$ and $I_{S,C}$ to the values in Table 1), which causes a transient spine enlargement. Four minutes after the stimulus was delivered, the spines settle to a new size with a shorter and wider neck (Fig. S12E) consistent with experimental observations (*12*, *17*, *25*).

When the stimulus is triggered, we observed that the number of barbed ends showed a rapid, initial increase followed by a slower rate of increase over time (Fig. S12F). The influx of proteins into the spine is responsible for the early rapid increase, while the later increase is due to the addition of barbed ends created by branching and severing events produced by the stimulus-triggered influx of ABPs. Note that cofilin and Arp2/3 total concentration increase at a decreasing rate due to their sequestering for the nucleation and branching events. After stimulation, the variables decay at rates similar to the experimental observations (*25*) (compare with Fig. S11A). These dynamics, informed by the parameter estimation (Fig. S11), effectively replicate the experimentally-observed protein dynamics.

We next calculated the change in the spine volume over time (Fig. 2D). The spine volume increase rapidly during the stimulus and settle to a new higher steady state value after the stimulus is turned off. This growth is consistent with the main features of sLTP, where the spine head size increases in response to a stimulus (*4*, *12*, *25*). We also measured the radius of the spine neck at the same height over time ($z \sim 0.47$ µm, see Fig. 2D). The spine neck radius increases upon LTP induction and keeps rising after the stimulus finishes until it reaches a new steady state with a radius 33.81% larger, consistent with (*12*). The spine shape change supports the difference between these increases (Fig. S12E). Moreover, the increase in spine volume is robust to variation of Arp2/3 and cofilin stimulus-triggered influx and disrupted when there is no stimulus-triggered actin influx (Fig. S14). Figure 2E shows the normalized variables of Figure S12F divided over the normalized volume. Interestingly, there is a 12-fold increase in the concentration of cofilin, which is higher than expected from the data in (*25*) (Fig. S11B). This could be caused by our assumption of a spatially homogeneous stimulus-triggered influx in the whole spine head. Overall, we found that our 3D model qualitatively replicates the temporal trends in spine volume and protein concentration observed in experiments (*25*).

To further inspect how the forces generated by the membrane and actin polymerization influence the shape evolution of the spine, we plotted the membrane mesh color-coded by the norm of these forces (Fig. S13A). As expected, the force generated by actin polymerization increased during the stimulation window but settled to a new steady state after 4 min, where the forces generated by actin polymerization are minimal. Throughout the simulation, the force generated by the membrane is higher at the spine neck rather than at the spine head. Note that the higher force in the spine neck arises from the smaller radius of the neck compared to the spine head radius. Moreover, there is a sharp change in curvature in the junction of the spine head and neck.

To quantify the evolution of the forces generated by the membrane and actin polymerization over time, we integrated the norm of the force vectors corresponding to each node of the spine membrane (Fig. S13B). During the stimulation window, the force generated by actin polymerization increased while the force generated by the membrane remained constant. We further analyzed this difference by obtaining the normalized change in the forces (Fig. 2K-M) and we observed an over three-fold increase in the force generated by actin polymerization upon stimulation (Fig. 2L). Note that this increase relates to that of barbed ends (compare Fig. 2E with Fig. 2L), as expected. Although the total force generated by the membrane does not increase during the stimulation win-

dow (Fig. 2K), the sum of the forces shows an increase (Fig. 2M), albeit a smaller one compared with that of the force generated by actin polymerization. Thus, we concluded that the force generated by the membrane reduces the force generated by actin polymerization only locally. After stimulation, the force generated by actin polymerization decays to a value smaller than that before stimulation, which also relates to the trend shown by the barbed ends. The forces fluctuate during this period due to the spatial variations. We observed that these fluctuations relate to an increase in the spine volume (Fig. 2D) and arise when the spine is settling into a new steady state. During this period, the number of barbed ends has greater enhancement at discrete locations, which translates into transient peaks of forces. The behavior of the membrane and actin polymerization forces is robust to changes in bending stiffness (see Supplementary Information S6, Fig. S15).

In our model, the increase of normalized cofilin concentration upon LTP stimulation is over seven times larger (Fig. 2E, thick line) than experimental observations (*25*) (Fig. S11B). Therefore, we examined whether a similar increase in spine volume could be achieved by localizing the influx of the ABPs, based on the observations that ABPs bind F-actin at different sites (*18*). Therefore, we proposed a compartmentalized stimulus-triggered influx. Because F-actin continuously polymerizes ATP-actin at the barbed ends and cofilin severs ADP-bound filaments (*20*), we restricted that cofilin activity to the region where the (-) ends of F-actin are located ($-7\Delta_x < \mathrm{d}(\mathbf{r}, t) < -3\Delta_x$). Since Arp2/3 binds at the barbed ends near the membrane (*20*, *33*, *51–53*), the influx-triggered Arp2/3 were located near the membrane ($-3\Delta_x < \mathrm{d}(\mathbf{r}, t) < -\Delta_x$). Additionally, we also localized the stimulus-triggered influx of actin into the spine ($-6\Delta_x < \mathrm{d}(\mathbf{r}, t) < -\Delta_x$). Figure 2B shows the distribution of the influx into the spine head (the stimulus height was restricted as before). Note that we have assumed that, upon stimulation, actin and ABPs rapidly flow into the spine and localize in the zones where they are most likely activated.

We found that with this compartmentalized influx, spines enlarge upon LTP induction (Fig. 2C) and cofilin concentration reduces at the end of the simulation (compare with Fig. S12E). Indeed, localized influx shows similar evolution of the normalized spine volume and neck radius (Fig. 2D), albeit with a reduction in the ABPs influx (Fig. 2E). Moreover, the forces locally show similar behavior after stimulation and at the end of the simulation (Fig. 2J). In short, the force generated by the membrane is higher in the neck while the force generated by actin polymerization is higher in the spine head just after the simulation. Quantification of the normalized integration of the forces over time shows similar values as those of the simulation with the homogeneous stimulus-triggered influx (Figs. 2K-M).

Since this compartmentalized influx reduces the increase of cofilin into the spine upon LTP induction and guarantees its usage, we predict that there must be a mechanism by which proteins are delivered to locations where they are most likely to be activated upon LTP induction, ensuring that resources are efficiently used. From here on, all simulations have compartmentalized stimulus-triggered influx.

We calculated the force-velocity for spine growth by calculating the membrane horizontal displacement at the middle of the spine head and measured the forces locally. The force-velocity relationships are shown in Figure 2G-I, for the forces generated by the membrane, actin polymerization and their sum. Consistent with other actin-mediated force-velocity relationships, we find that the velocity is higher for smaller forces (*54*, *55*), except for the force generated by actin polymerization (Fig. 2H) that has its maximum at medium force values. This is in line with our assumption that the force generated by actin polymerization drives spine protrusion. Thus, we predict that spine growth during sLTP follows the force-velocity relationships and captures the well-established behaviors of actin-membrane interactions.

We observed that the evolution of the spine volume resembles the strain response of a viscoelastic material to a load despite the multiple chemical and mechanical features in the model

(Fig. 2F). To examine the mechanical properties of the spine in our model, we fitted a Kelvin-Voigt model, composed of a spring and a dashpot connected in parallel (see Supplementary Information S2.3 for details). We found that the volume evolution fit this viscoelastic description very well (squared norm of the residual = 0.0196) with a dashpot viscosity of $\upsilon = 123.6755$ pN s/μm and a spring constant of $R = 0.0967$ pN/μm (Fig. 2F). Thus our model predicts that the high dashpot viscosity and the lower spring constant allow the spine to behave like a fluid upon induction of LTP, promoting spine enlargement.

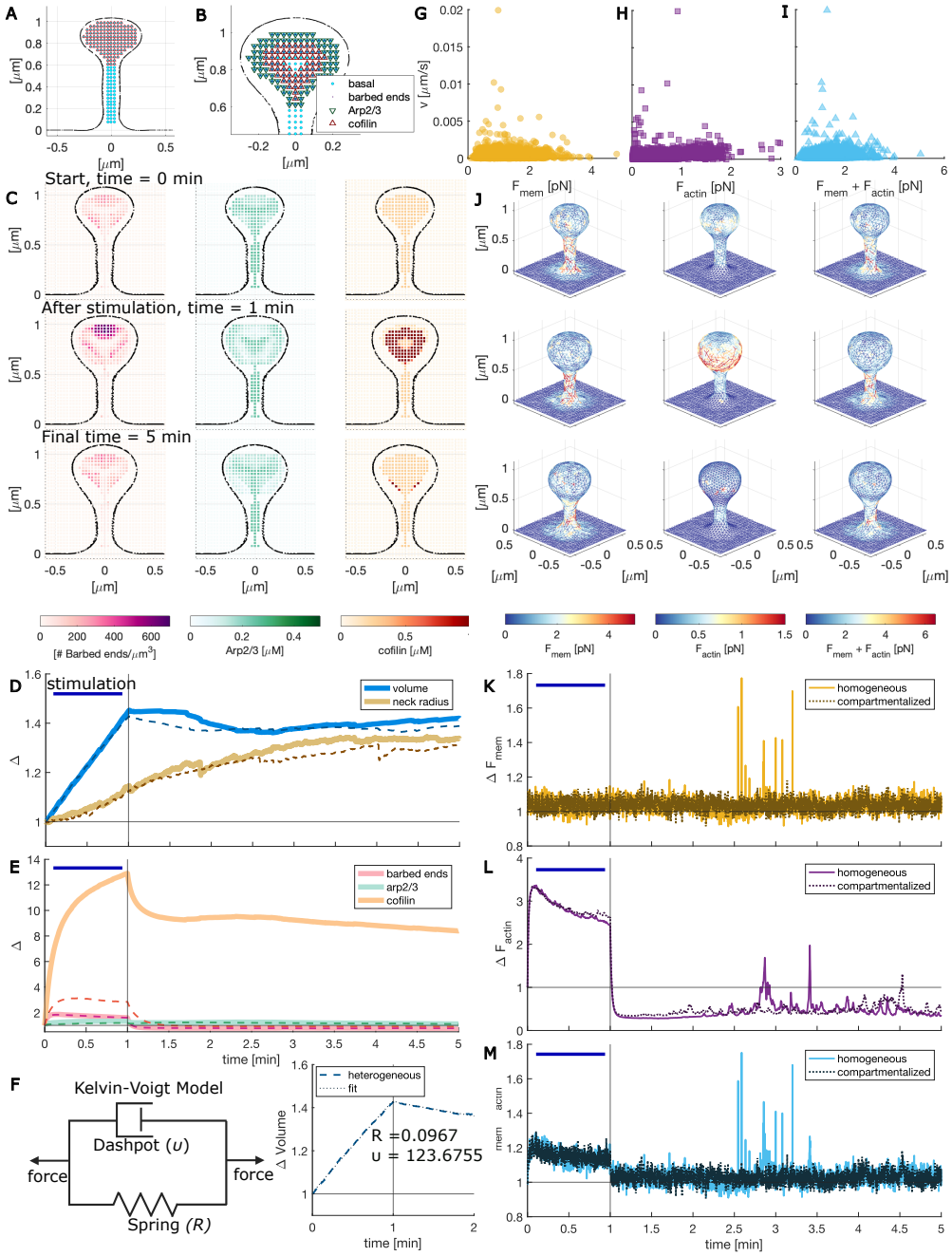

Figure 2: Compartmentalized stimulus-triggered influx A) Slide of a dendritic spine at $x = 0$ µm showing the spatial locations of basal influx (cyan circles) and stimulus-triggered influx (red triangles). Note that the red triangles overlap the cyan circles, and that the stimulus-triggered influx is homogeneous in the spine head. **B**) Scheme of actin and ABPs influx spatial distribution in the compartmentalized case. **C**) Snapshots of the spines, slide at $x = 0$ µm showing the spatio-temporal dynamics of the number of barbed ends and the concentration of Arp2/3 and cofilin at the start of the simulation (top), after stimulation (center), and at the end of the simulation (bottom). See movie S2 for the full evolution. **D**) Normalized volume and spine neck radius evolution over time for the models with homogeneous (solid line) and compartmentalized (dash-dotted line) stimulus-triggered influx. **E**) The normalized number of barbed ends and Arp2/3 and cofilin concentration in the spine corresponding to the homogeneous (solid line) and compartmentalized (dash-dotted line) model. **G-I)** Plot of the protrusion velocity over force generated by the membrane, actin polymerization, and both, respectively. The protrusion velocity was calculated as the horizontal displacement of the membrane at the middle of the spine head. The force was taken locally, i.e., the force corresponding to the triangular face that intersects the displacement vector. **J**) Dendritic spines at the start of the simulation (top), after stimulation (center), and at the end of the simulation (bottom) color-coded for $F = ||\mathbf{F}||$. **K-M**) Evolution of the normalized force generated by the membrane, actin polymerization, or both with the homogeneous and compartmentalized influx.

4.2 Repeated LTP inductions lead to a reduction in spine growth rate

Since synapses receive a series of stimuli (*56*), we next investigated what would happen to spine enlargement upon repeated LTP inductions. To do so, we simulated repeated LTP inductions: the first at the start of the simulation, the second at minute 2, and the third at minute 4. Thus, the spine was stimulated for one minute (i.e., $I_S > 0$ in Eqs. 1, 7, and 8) and let to rest for the following minute. We chose this stimulation protocol because the spine volume settles to a steady state after one-minute rest (see Fig. 4E, thick line).

We observed an increase in the size of the spine head and a shortening and widening of the spine neck at the end of each stimulus (Fig. 3A). At the end of the simulation, the amount of cofilin remaining in the spine increased when compared to a single stimulus (Fig.2D). The spine normalized volume and neck radius increased with every LTP induction (Figs. 3B-C). Interestingly, the peak of the normalized number of barbed ends per μm^3 was smaller after each stimulus, while the peak in normalized cofilin concentration was higher in the last stimulus (Fig. 3D). The normalized concentration of Arp2/3 increased after the first stimulus but decayed at different rates during the following stimulation windows (Fig. 3D). To have a better comparison of the different decays, we re-plotted the quantities by normalizing their values to the value at the start of each LTP induction. Figure 3E shows that the increase of the volume is smaller after each stimulus. Interestingly, the peak of the number of barbed ends increased after each stimulation (Fig. S5B) that could arise from nuclation and severing events leading to the decrease of Arp2/3 and cofilin, respectively (Figs. S5C-D).

We next investigated whether the mechanical properties of the spine changed by fitting a Kelvin-Voigt model to the volume trace for each stimulus (Fig. 3E). In the second stimulus, the spring constant and the dashpot viscosity increase ($R = 0.1056$ pN/μm, $\upsilon = 159.6712$ pN s/μm, squared norm of the residual = 0.0476) compare to the first stimulus ($R = 0.0967$ pN/μm, $\upsilon = 123.6755$ pN s/μm, squared norm of the residual = 0.0196), which suggest a stiffening of the spine. Experimental observations link similar stiffening (or increase in spring constant) with spine maturation and stabilization (*28*). However, in the third stimulus, the spring constant decreases while the dashpot viscosity increases ($R = 0.0152$ pN/μm, $\upsilon = 259.9553$ pN s/μm, squared norm of the residual = 0.0101). We predict that such behavior indicates a homeostatic mechanism by which spines first mature and stabilized, but after repeated LTP inductions, the protein density in the spine saturates (high υ), inducing structural destabilization by reducing R.

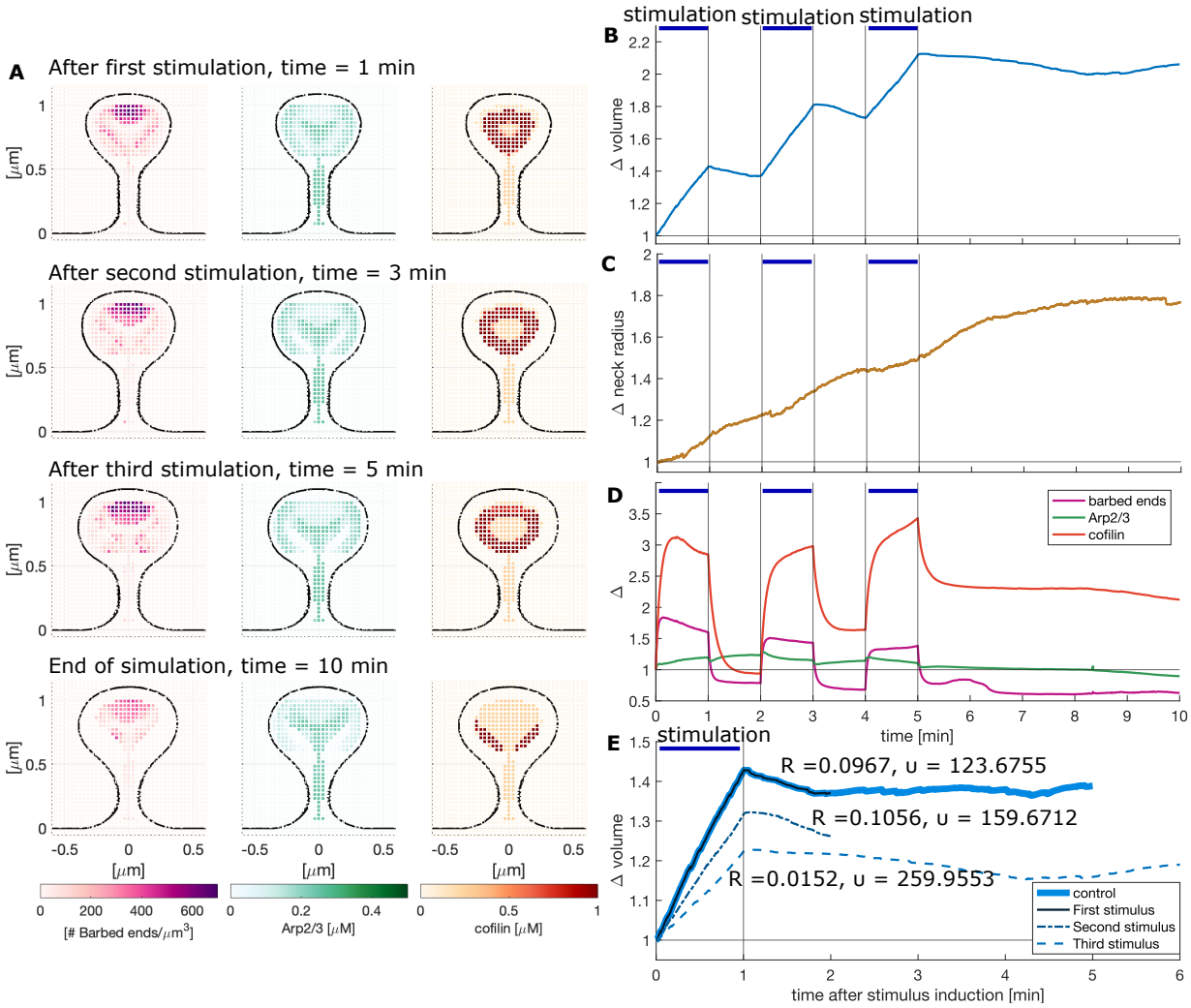

Figure 3: Effect of repeated LTP inductions in protein spatial distribution. A) Snapshots of a slide of a dendritic spine at $x = 0$ μm showing the spatio-temporal distribution of the number of barbed ends, Arp2/3 and cofilin. See movie S3 for full evolution. **B**) Normalized volume evolution over time. Different simulations are marked with a blue horizontal line. **C**) Normalized spine neck radius evolution over time. **D**) Normalized number of barbed ends per micron and Arp2/3 and cofilin concentration in the spine. **E**) Evolution of the normalized volume to the start of each stimulus and the respective fits to a Kelvin-Voigt model.

The forces generated by the membrane were higher at the spine neck while the forces generated by actin polymerization were concentrated at the spine head (Fig. 4A). We note that these localized forces are greater at the end of the first LTP induction and lower at the end of the simulation. The peak of the total normalized forces during the stimulation window decreases over time (Fig. 4B). However, when we took the normalization with respect to the start of each stimulation, we observed that the force generated by actin is higher during the second stimulus (Fig. 4D). Although there is no visible change in the force generated by the membrane (Fig. 4C), the total force remains lower than in the first stimulus (Fig. 4E), following the same trend as the volume (Fig. 3B). Taken all together, the change in the trends of the normalized protein concentration and forces hint at a complex relationship between the stimulus-triggered influx and the spine volume. In our simulation, spine enlargement was dependent on the spine size at the start of the LTP induction: larger spines showed reduced size increase, as in experimental data (*4*, *57*), despite the increase in the number of barbed ends. By modulating their viscous and elastic properties, dendritic spines

may harness their mechanical features to adapt to multiple stimuli. Thus, we conclude that the spine self-regulates its growth by tuning the mechanical responses.

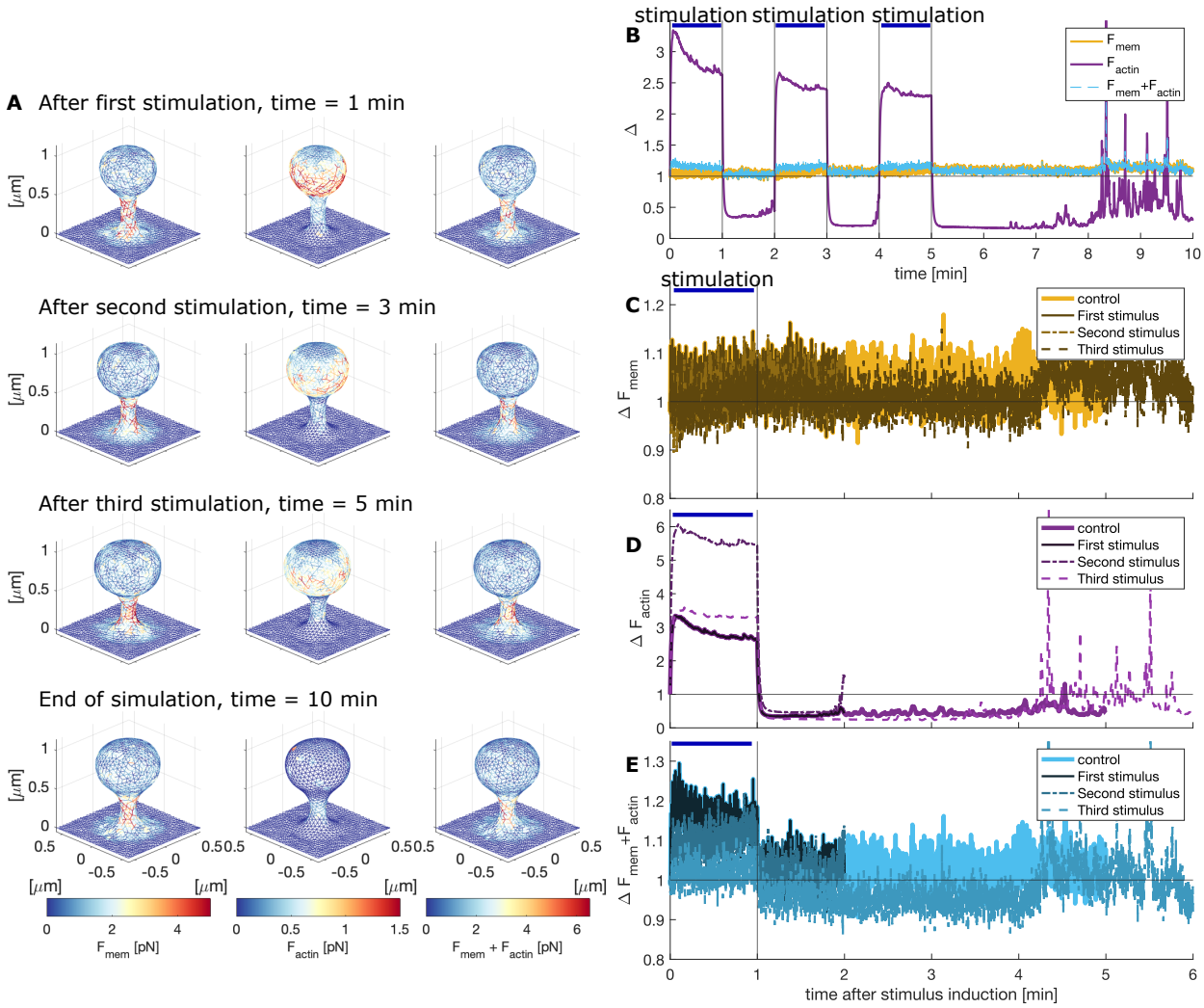

Figure 4: Effect of repeated LTP inductions in forces A) Snapshots of the dendritic spine mesh at different times with edges are color-coded for the norm of the force vector $F = ||\mathbf{F}||$. **B**) Temporal evolution of the integral of the forces normalized to the initial value. **C-E**) Temporal evolution of the integral of the force generated by the membrane, actin polymerization, or both, normalized to the value at the start of each stimulus.

4.3 Mechanical forces from clutch molecules promote spine enlargement

Recent experimental results show that coupling F-actin with the extracellular space via clutch molecules is necessary to achieve spine enlargement upon LTP (*29*) (Fig. 5A). This clutch coupling is thought to reduce the retrograde flow of F-actin and increase the force generated by actin polymerization (*29*). Here, we investigated the impact of such coupling on volume growth. To simulate the reduction of retrograde flow, we decreased the value of the effective filament mobility η in Eq. (2). We found that decreasing η increased the volume of the spine (Fig. 5B-C). Reducing η by 50% increases the peak of the normalized volume from 1.4288 to 1.6192. However, we found that the relationship between η and the peak of spine volume is nonlinear (Fig. 5D). When the retrograde flow decreases, the maximum of the normalized number of barbed ends in the spine increases (Fig. S6B) while the normalized concentration of Arp2/3 and cofilin decreases (Fig. S6C-D). Thus,

we conclude that when the retrograde flow decreases, the nucleation, and severing of F-actin increases. The higher the force generated by actin, the larger the peak of the normalized volume (Fig. S6F), indicating that the reduction of the retrograde flow enhances the force generated by actin polymerization, which promotes spine growth.

Next, we obtained the spring constant and dashpot viscosity for the different values of η. Interestingly, the spines with the reduced retrograde flow by 50 and 60% show an increase in both values when decreasing retrograde flow, thereby increasing the peak volume (Figs. 5E-F). We predict that the increase in the spring constant and dashpot viscosity is related to a more robust stabilization by the action of clutch molecules upon LTP induction. For the other values of η, there is no clear trend, indicating a possible threshold for spine stabilization. Taken together, we predict that mechanical forces from clutch molecules enhance spine volume increase by increasing the force generated by actin polymerization and perhaps the enhancement of barbed ends due to the nucleation and severing events. This translates to robust stabilization due to the changes in the mechanical properties of the spine.

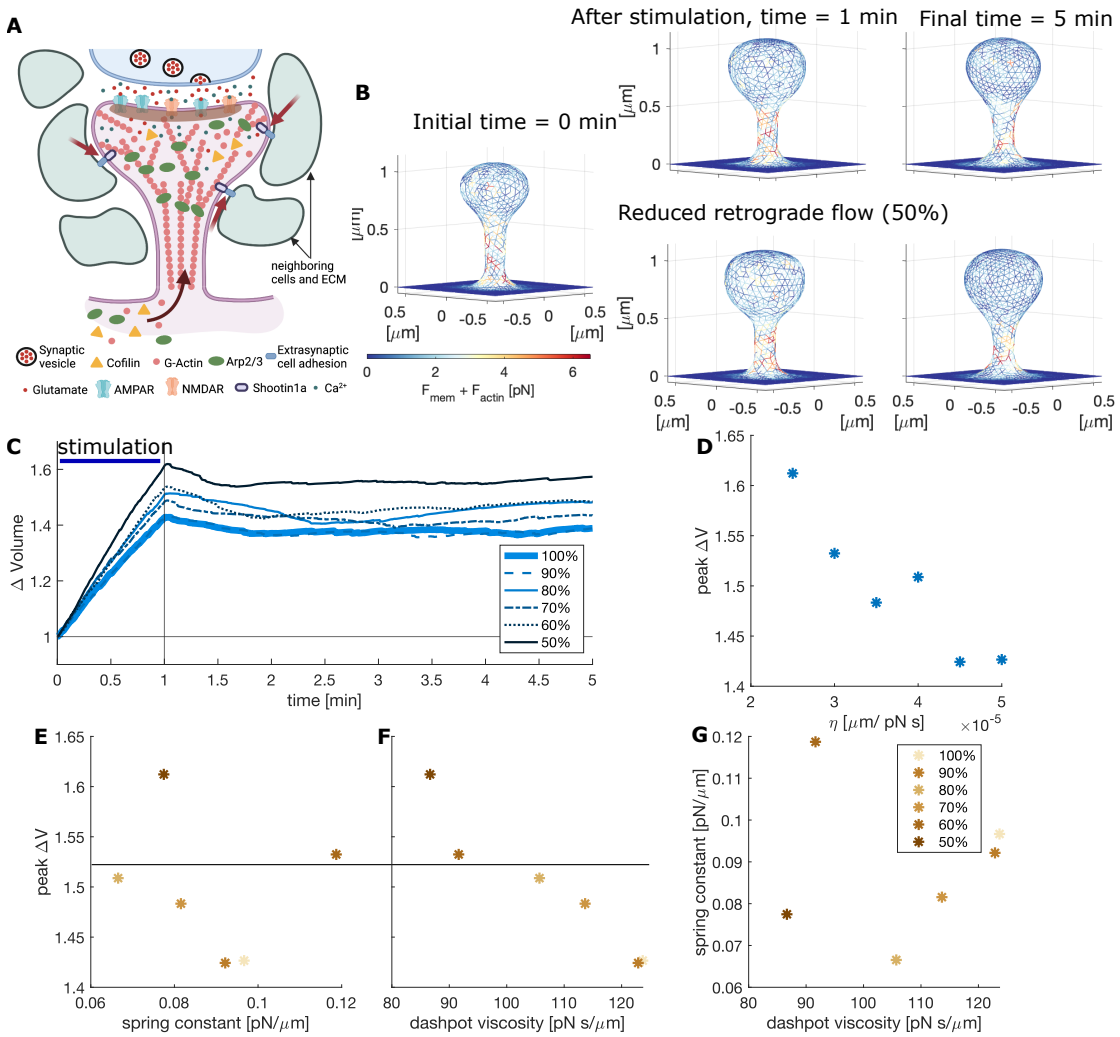

Figure 5: Influence of clutch molecules in dendritic spines. A) Schematic depiction of coupling between F-actin and ECM and neighboring molecules by shootin1a (red arrows). Image created with `BioRender.com`. **B)** Snapshots of the dendritic spine mesh at different times with normal (top) and reduced (50%, bottom) retrograde flow. Edges are color-coded for the combination of the forces generated by the membrane and actin polymerization. For full evolution see Movie S4. **C)** Normalized spine volume evolution over time. Different line types correspond to the scale of retrograde flow in the model. **D)** Normalized volume at the end of the stimulation window (peak volume) for different values of retrograde flow η. Peak volume against the spring constant (**E**) and dashpot viscosity (**F**) for different values of η. **G)** spring constant against dashpot viscosity for different values of η. The squared norm of the residuals are: 0.1435 (50% η), 0.0660 (60% η), 0.0914 (70% η), 0.0383 (80% η), 0.0160 (90% η), and 0.0196 (100% η).

5 Discussion

In this work, we developed a 3D computational model for sLTP in a dendritic spine. Our model accounts for the spatial localization and chemical reactions of actin barbed ends, Arp2/3, and cofilin, and their interactions with the spine membrane. Computationally, to our knowledge, this is the first 3D model that allows simultaneous protein temporal and spatial evolution, described by partial differential equations (PDEs) in a moving boundary framework, leading to asymmetric shape changes for sLTP. For purposes of computational tractability, we only focused on a few key ABPs.

Our model is able to capture the key experimentally observed features of spine expansion due to a stimulus under different conditions. We observe an increase in the barbed ends, spatial effects of Arp2/3, and cofilin activity, and note that the dynamics of these species qualitatively match experimental observations. Since the kinetic parameters of these species were experimental data (*25*), our model predictions represent plausible dynamics. Additionally, the spatiotemporal maps give us a sense of how these molecules may arrange themselves in the spine during active remodeling. It is possible that there may be mislocalization of the proteins in the experiments due to the challenges associated with the overexpression of recombinant proteins fused to GFP (*58*), resulting in miscalibration. Nonetheless, the main dynamic events of increase in actin barbed ends and the net force generated are consistent with the literature (*34*, *59*). We chose ABPs that capture minimal actin remodeling events (*18*, *20*) and because these proteins are important for healthy brain function. For example, failure of Arp2/3 function leads to spine loss and abnormal synaptic function, enhancing excitation and leading to similar symptoms to psychiatric disorders (*60*), and experimental studies indicate that cofilin is involved in Alzheimer's disease synaptic dysfunction (*61*).

The force-velocity relationships predicted from our model are consistent with other actin-mediated force velocity relationships (*34*, *54*, *55*). The spatial nature of our model allowed us to investigate the force distribution along the spine membrane and found that the membrane force is highest at the neck. Importantly, in our model, the neck becomes wider and shorter after LTP induction, as observed in experimental data (*12*), hinting that changes in the spine neck could be driven by membrane forces. Although we did not consider the effect of the periodic actin rings in the neck (*62*), we observed that the neck retained its cylindrical structure. Future extensions of our work could explore a previously suggested theoretical hypothesis suggesting that such rings reduce the total membrane energy of the spine (*63*).

We observed that while the relationships between the protein concentration, force generation, and volume increase are complex, they are best captured by simple viscoelastic models. We predict that the spine acts as a viscoelastic object – by tuning the spring constant and dashpot viscosity under different conditions, spines are able to translate different actin-related biochemical events into mechanical events. As a result of this viscoelastic behavior, spines are able to modulate their response to multiple stimuli using spine stiffening as mechanical response. Our model predictions are in line with experimental data showing that larger spines experience less volume increase upon LTP (*4*). This volume saturation is thought to be regulated by homeostatic mechanisms (*64*), where the spine regulate its synaptic strength by increasing or decreasing the number of AMPARs or NMDARs at the PSD. It has been shown that dendritic spines that experience these homeostatic mechanisms show larger volume increases upon LTP induction (*57*). Here we show that such homeostastis may be achieved by tuning the spring constants and dashpot viscosities (Fig. 6).

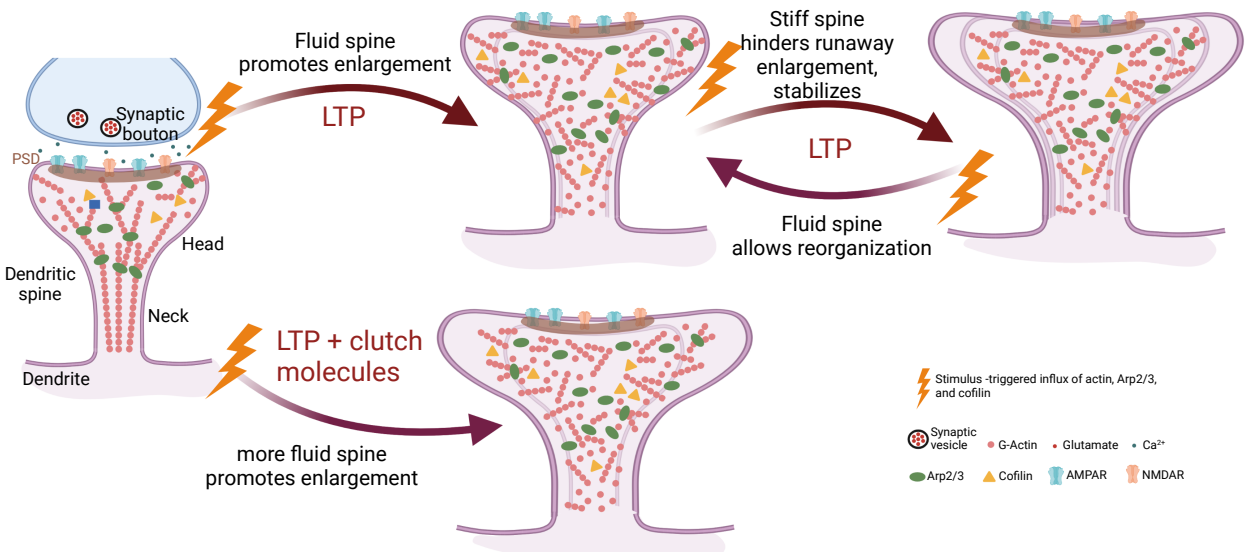

Figure 6: Evolution of the viscoelastic properties of the dendritic spine. Summary of the main predictions from our model for the change in the mechanical properties of the spine and how this may regulate the balance between spine growth and spine stabilization. Created with `BioRender.com`

Further tuning of these mechanical properties can be achieved by modulating the retrograde flow of barbed ends. Recent experimental data found that the clutch molecules, which couple F-actin with the extracellular space, reduce the speed of the retrograde flow and hence, promote the actin polymerization force driving spine enlargement (*29*). When the coupling with F-actin was disrupted, polymerization of F-actin increased the retrograde flow (*29*). In our model, we observed a threshold in the value of retrograde flow, where further reduction of the retrograde flow decreases the spring constant and dashpot viscosity of the spine during LTP, thereby destabilizing the spine. We predict that this is a homeostatic mechanism that maintains the spine within physiological size.

In this work, we focused on the biophysical aspects of spine growth but did not include the signaling events that are a part of the process (*65–67*). These signaling events are known to be regulated by the spine shape (*67–69*). In future work, our framework can be extended to include these upstream signaling events and downstream receptor trafficking events. Furthermore, because simulations involved the whole cubic domain, presynaptic and perisynaptic elements can be added at some computational cost. Recent progress in analysis of moving boundary problems could elucidate an understanding of the relationship between model parameters and its dynamics (*70*). In summary, we have shown that the biochemical events associated with actin remodeling result in a fine tuning on the mechanical properties of spine viscoelasticity, and tuning this viscoelasticity offers a potential pathway for the regulation of learning and memory formation. We anticipate that this work will set the stage for coupled modeling and interrogation of the biochemical and mechanical events of sLTP in closer proximity than before.

Acknowledgements

This work was supported by the NIH Grant Number 1RF1DA055668-01 and by an Air Force Office of Scientific Research Grant FA9550-18-1-0051 to P.R. We thank members of the Rangamani Lab and members of the Le BIP MURI for fruitful discussions. We thank Dr. Christopher Lee, Maria Hernandez Mesa, and Sarida Pratuangtham for their edits and comments.

Supplementary Information

Figure S1: Movie S1: Protein temporal and spatial evolution upon LTP. Cross section of the dendritic spine at $x = 0$ µm showing the value of the number of barbed ends (left), Arp2/3 (center) and cofilin (right) concentrations. Volume and surface area evolution. Movie corresponding to Figure S12.

Figure S2: Movie S2: Compartmentalized stimulus-triggered influx. Cross section of the dendritic spine at $x = 0$ µm showing the value of the number of barbed ends (left), Arp2/3 (center) and cofilin (right) concentrations. Volume and surface area evolution. Movie corresponding to Figure 2.

Figure S3: Movie S3: Effect of repeated LTP inductions in protein spatial distribution. Cross section of the dendritic spine at $x = 0$ µm showing the value of the number of barbed ends (left), Arp2/3 (center) and cofilin (right) concentrations. Volume and surface area evolution. Movie corresponding to Figure 3.

Figure S4: Movie S4: Influence of clutch molecules in dendritic spines. Cross section of the dendritic spine at $x = 0$ µm showing the value of the number of barbed ends (left), Arp2/3 (center) and cofilin (right) concentrations. Volume and surface area evolution. Movie corresponding to Figure 5.

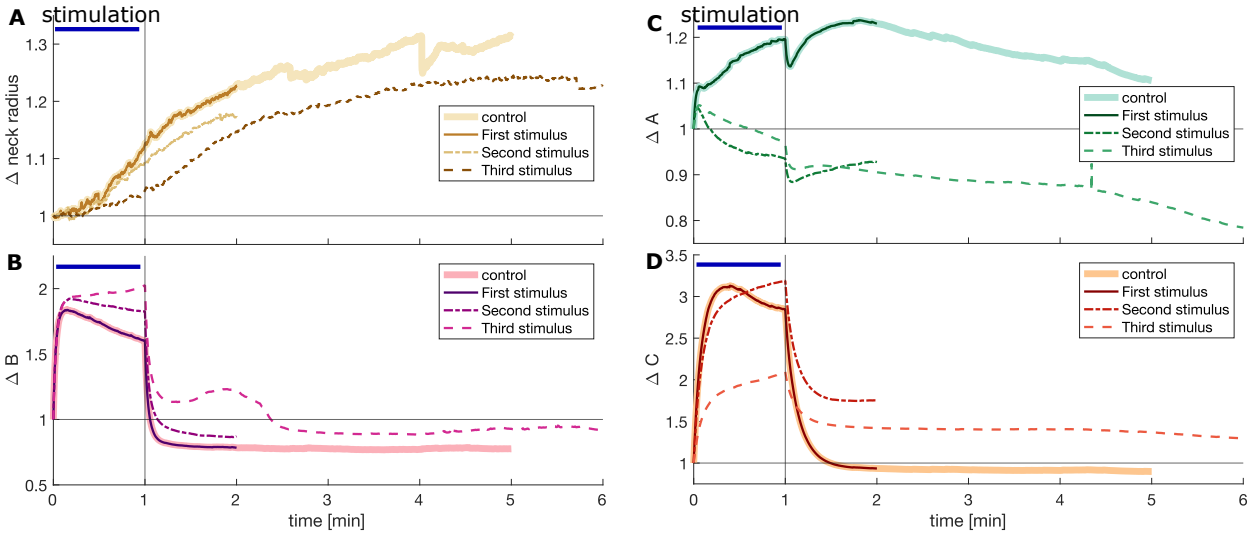

Figure S5: Effect of repeated LTP inductions in protein spatial distribution. Evolution of the normalized spine neck radius (**A**), number of barbed ends per micron (**B**), and Arp2/3 (**C**) and cofilin (**D**) concentrations to the start of each stimulus.

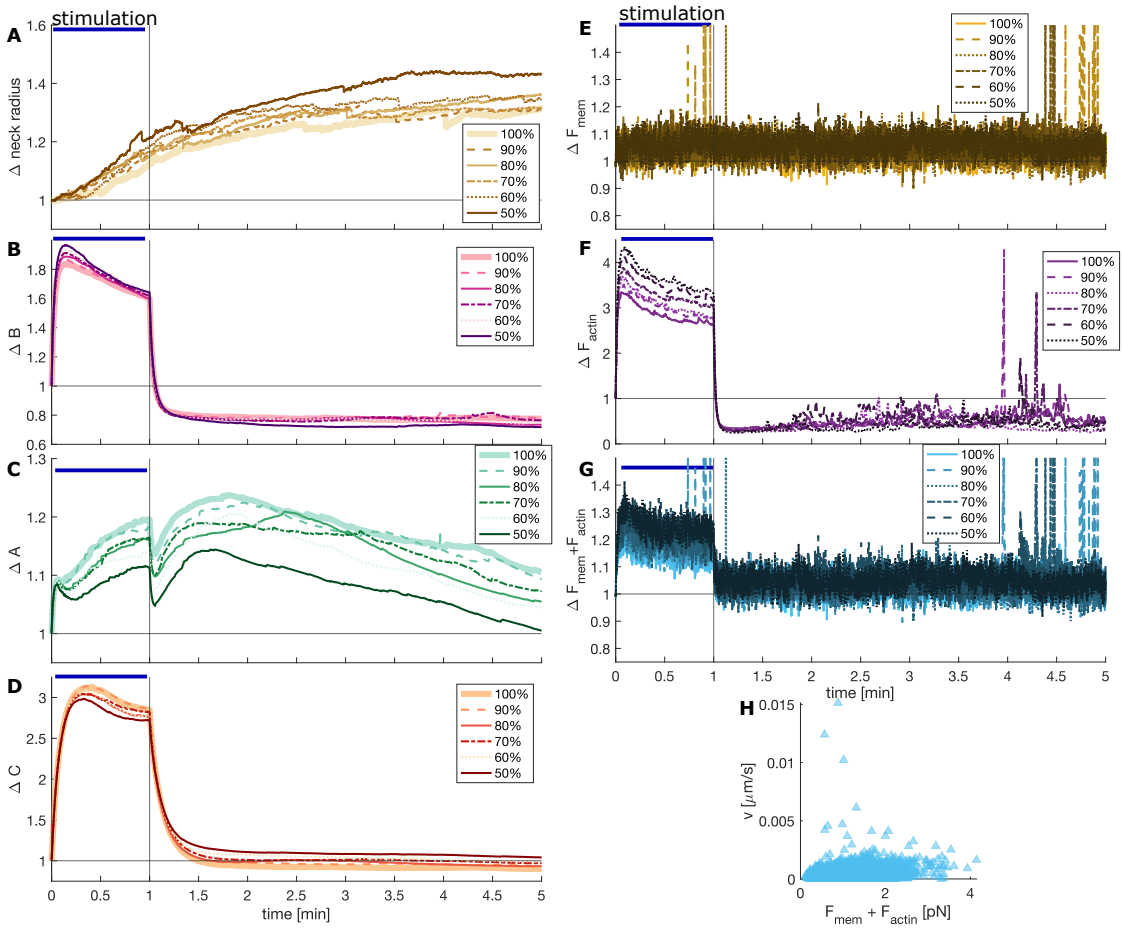

Figure S6: Influence of clutch molecules in dendritic spines. A) Normalized neck radius evolution over time. **B-D)** Change in normalized barbed ends and ABPs concentration over time. **E-G)** Change in the normalized integral of the forces generated by the membrane, actin polymerization, and both. **H)** Force-velocity relationship for the different types of forces.

S1 Membrane Discretization

In our model the dendritic spine is embedded in a cubic domain $\mathcal{L}$ (Fig. S7A). In this section, we present the discretized version of the continuous system used in the main text. Figure S7D shows the mesh corresponding to the discretized $\mathcal{L} \in \mathbb{R}^3$ cubic domain with a uniform spacing Δ_x. Note that we use concentration of Apr2/3 and cofilin, or number of barbed ends per volume (Fig. S7C) instead of modeling the structure of the dendritic spine cytoskeleton (Fig. S7B). The points of the cubic domain mesh $\mathbf{r}$ remain constant over the simulation. A triangular mesh that represents the spine membrane is embedded in this cubic domain (Fig. S7E). The position of the nodes of the spine mesh $\mathbf{s}$ change at each time-step according to Eq. (9) (see Figure S8 for the simulation flowchart).

In order to track the relative position of $\mathbf{r}$ with respect to the spine membrane, we define a signed distance function. Thus, for the points laying outside the membrane, the distance is positive, and negative otherwise (Fig. S9A). The distance $\mathrm{d}(\mathbf{r}, \Gamma)$ corresponds to the minimum distance from the lattice point $\mathbf{r}$ to the hexagonal mesh representing the membrane Γ. For its calculation, there are two cases (Fig. S9B):

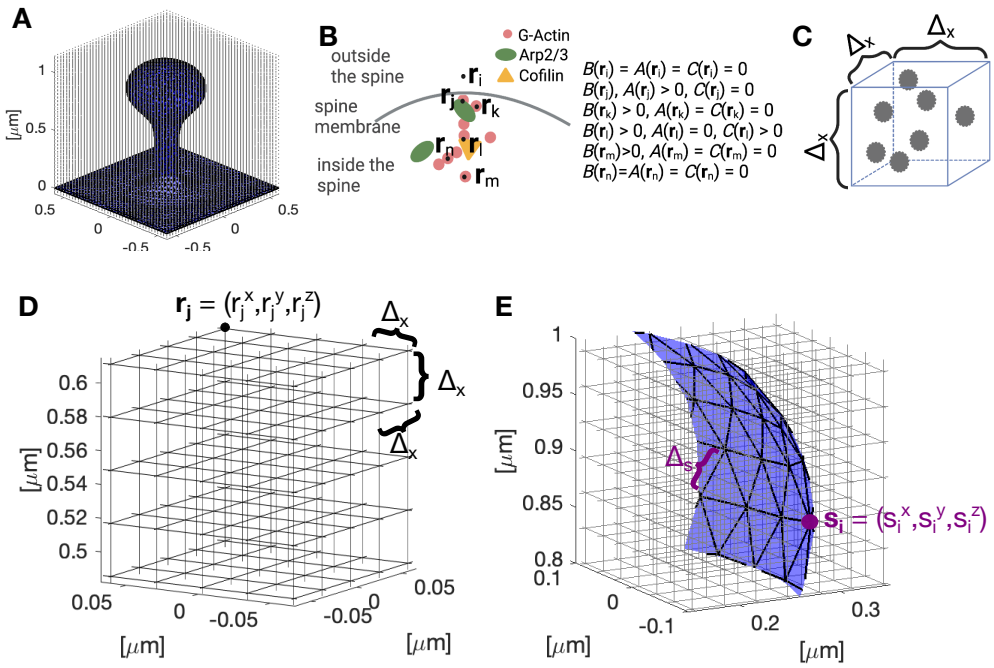

Figure S7: Discretization of simulation. A) Dendritic spine (blue mesh) embedded in a cubic domain $\mathcal{L}$. Dots correspond to the positions **r** (the discretization of this domain). **B)** We assume a given concentration of Arp2/3, cofilin and number of barbed ends per discretized volume (**C**), instead of modeling the individual filaments. **D)** Zoom to the cubic domain $\mathcal{L}$, discretized in intervals of length Δ_x. The intersection of the grid lines correspond to the discretized positions $\mathbf{r}$. **E)** Zoom of the spine membrane (in blue) embedded in the cubic domain. This membrane is discretized using a triangular mesh, where the nodes positions $\mathbf{s}$ are time evolving.

1. The closest point to the membrane from $\mathbf{r}$ is a vertex $\mathbf{s}$. Then,

$$\mathrm{d}(\mathbf{r}, \Gamma) = \sqrt{\mathbf{v} \cdot \mathbf{v}}, \quad \mathbf{v} = \mathbf{r} - \mathbf{s}. \tag{S1}$$

2. The closest point to the membrane from $\mathbf{r}$ is the triangular face i that spans through the vertices $(\mathbf{s}_i, \mathbf{s}_{i+1}, \mathbf{s}_{i+2})$. Then,

$$\mathrm{d}(\mathbf{r}, \Gamma) = |\mathbf{v} \cdot \mathbf{n}_i|, \quad \mathbf{n}_i = \frac{\mathbf{N}_i}{\sqrt{\mathbf{N}_i \cdot \mathbf{N}_i}}, \quad \mathbf{N}_i = (\mathbf{s}_{i+1} - \mathbf{s}_i) \times (\mathbf{s}_{i+2} - \mathbf{s}_i), \tag{S2}$$

where $\mathbf{N}_i$ is the normal vector (Fig. S10) and $\times$ represents the cross product.

In our numerical implementation, the normal vector to the mesh surface points to the outside of the spine, and the bulk flow direction is $-\mathbf{v}$. This is considered in the calculations by changing the signs accordingly.

For the calculation of the force generated by the membrane $\mathbf{F}_{mem}$ (Eq. 12), we follow (*43*, *71*) and take the discretization of the Helfrich bending energy

$$\mathcal{E}_b = \frac{\kappa}{2} \int_\Gamma \mathrm{d}A H^2 \tag{S3}$$

given by

$$\mathcal{E}_b \approx \tilde{\kappa}_B \sum_{i,j} (1 - \cos\theta_{ij}), \quad \cos\theta_{ij} = \mathbf{n}_i \cdot \mathbf{n}_j, \quad \tilde{\kappa}_B = \sqrt{3}\kappa, \tag{S4}$$

where $\mathbf{n}_i$ is the unit normal vector of the i triangular face. As depicted in Figure S10, θ_{ij} is the is the angle formed between two adjacent triangles.

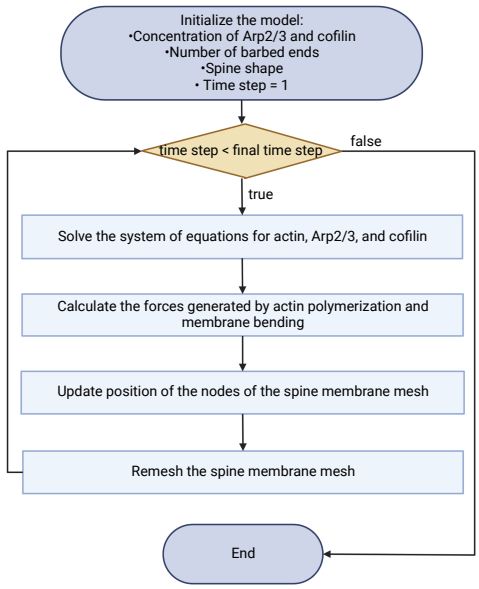

Figure S8: Flowchart outlining the key steps of the simulation.

We use a similar implementation as in (*72*, *73*). In short, we calculate the derivatives of Eq. S4 with respect to the membrane mesh vertices $\mathbf{s}$ to obtain the membrane force $\mathbf{F}_{mem}$ at each time-step. To obtain the initial spine shape, we initially construct a mesh with a spheroid connected to the x-y plane representing the membrane via a cylinder, which represents the spine neck. To obtain a stable shape, we let the position of the vertices evolve according to Eq. (9), but only considering the force generated by the membrane (i.e., $\mathbf{F}_{actin} = \mathbf{0}$). We anchor the spine to the dendrite by fixing the vertices corresponding to the dendrite (magenta points in Fig. S12A).

S2 Parameter Estimation

S2.1 Scale Factors

To convert the concentrations of β-actin to number of barbed ends per μm^3, we assume that there are 167 G-actin per F-actin since the mean length of dynamic F-actin in dendritic spines is around 450 nm (range: 200 - 700 nm (*16*)) and a monomer of actin contributes to 2.7 nm of the filament length (*34*). To change from number of molecules to μM, we use Avogadro's number and obtain $\Psi_0 \approx 3.6$ number of barbed ends $/(\mu\text{m}^3\mu\text{M})$. To convert number of barbed ends per μm^3 to concentration of Arp2/3, we follow (*32*) and assume that there is a minimal distance of 37 nm between branches of a filament. Hence, there are 12 molecules of Arp2/3 per F-actin, which gives a scale factor of $\Psi_1 \approx 0.02\mu\text{m}^3\mu\text{M}/$ number of barbed ends.

S2.2 Protein Dynamics

We obtain the data points from Figure 1 in (*25*) by annotating the plots in Fiji (*74*) with the multi-point tool. This figure shows the volume (RFP) and amount of GFP protein were quantified by the relative fluorescence intensity (F) to the average baseline (F0). These points are exported to Matlab (*45*) using the `ReadImageJROI.m` function (*75*). After scaling the points to the corresponding

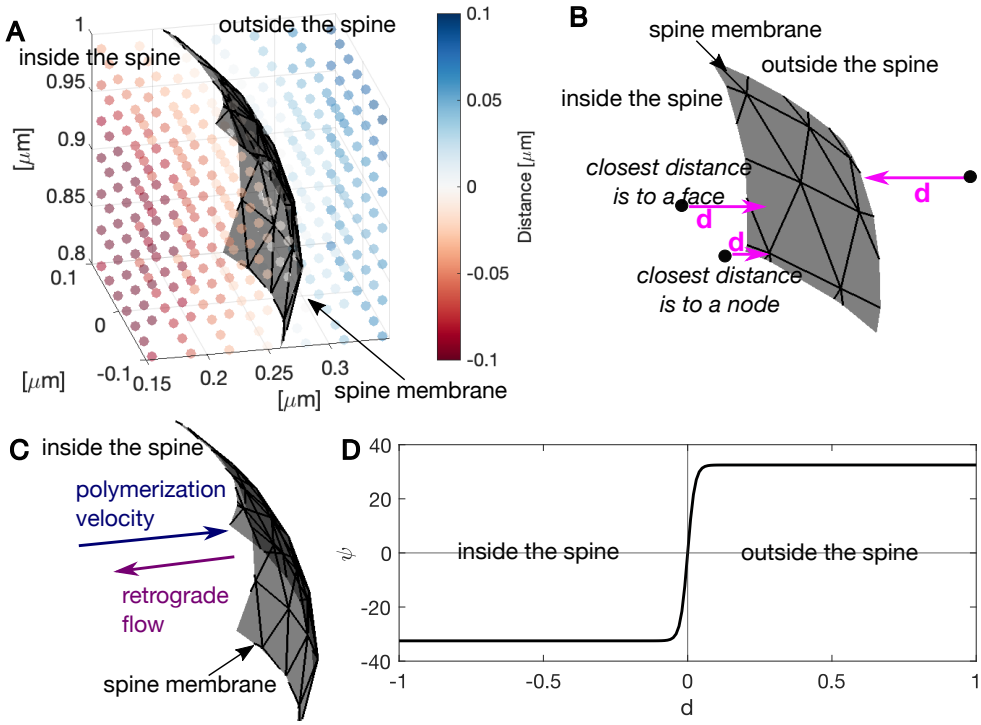

Figure S9: Distance functions A) Zoom of the simulated domain. Each dot represent a position $\mathbf{r}$, color-coded to the signed distance from the membrane (gray mesh). **B**) Scheme of the different cases for calculating the distance to the spine membrane. **C**) Scheme of the different actin forces. **D**) Plot of the function ψ in Eq. (4).

scale set in Fiji, we calculate the normalized concentration of the proteins as the ratio between the protein fluorescence intensity and the spine volume, as in (*25*) (markers in Fig. S11).

For estimation of the parameters corresponding to the actin, cofilin, and Arp2/3 influx into the dendritic spine upon LTP, we develop a minimal model that assumes that these proteins are continuously entering and exiting the spine. Moreover, we consider protein degradation and recent experimental findings that show that some proteins, like β-actin, are synthesized locally in the spine (*37*, *38*). For simplicity, we have gathered the continuous protein influx and synthesis in a source term I, and the efflux and degradation in a decaying rate k. Besides these continuous fluctuations, we consider a protein influx triggered by LTP induction $I_S(t)$, which is only present during the glutamate uncaging (1 minute). For simplicity, we assume that $I_S(t)$ are constant values and that during the stimulus window corresponding to the 1 minute glutamate is uncaging $I_S(t) > 0$, $I_S(t) = 0$ otherwise. Hence, in this minimal model, the dynamics for the normalized concentrations of β-actin (β), Cofilin-1 (C), and Arp2/3 (A) are given by

$$\begin{aligned} \frac{\mathrm{d}\beta}{\mathrm{d}t} &= I_{S,\beta}(t) + I_\beta - k_\beta \beta, \\ \frac{\mathrm{d}A}{\mathrm{d}t} &= I_{S,A}(t) + I_A - k_A A, \\ \frac{\mathrm{d}C}{\mathrm{d}t} &= I_{S,C}(t) + I_C - k_C C. \end{aligned} \tag{S5}$$

To reduce the number of parameters and guarantee that the pre-stimulus (i.e., $I_{S,\beta}(t) = I_{S,A}(t) = I_{S,C}(t) = 0$) level of protein concentration equals one for all the proteins, we first calculate the steady state of the system $(\beta^*, A^*, C^*) = (I_\beta/k_\beta, I_A/k_A, I_C/k_C)$. Then, we scale the system using

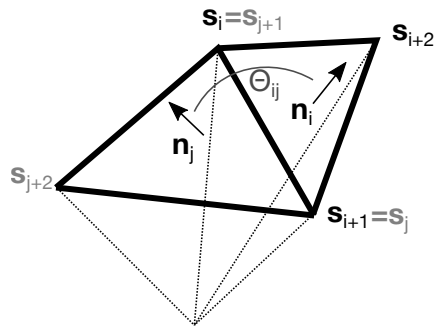

Figure S10: Geometrical components of the triangular mesh. Two adjacent triangles. Note that the position of the nodes $\mathbf{s}_i$, $\mathbf{s}_{i+1}$, and $\mathbf{s}_{i+2}$ is layout in a counterclockwise manner. This guaranties that the unit normal vector $\mathbf{n}_i$ points outside the mesh. The adjacent triangle j shares two nodes with the triangle i, but they have different order in the triangulation. The angle between these two adjacent triangles is θ_{ij}.

the nondimensional quantities $(b(t), a(t), c(t)) = (\beta(t)/\beta^*, A(t)/A^*, C(t)/C^*)$, which gives

$$\begin{aligned} \frac{\mathrm{d}b}{\mathrm{d}t} &= \frac{I_{S,\beta}(t)}{\beta^*} + k_\beta\,(1-b) \\ \frac{\mathrm{d}a}{\mathrm{d}t} &= \frac{I_{S,A}(t)}{A^*} + k_A\,(1-a)\,, \\ \frac{\mathrm{d}c}{\mathrm{d}t} &= \frac{I_{S,C}(t)}{C^*} + k_C\,(1-c)\,. \end{aligned} \tag{S6}$$

We fit the data points from (*25*) to the solutions of Eqs. (S6) with the `lsqcurvefit` function in Matlab to obtain the values of the efflux rate constants: k_β, k_A, and k_C; and the influxes upon LTP: $I_{S,\beta}(t), I_{S,A}(t)$, and $I_{S,C}(t)$. We use the `ode45` solver to evolve the system in Eqs. (S6). Figure S11B shows the resulting fit (squared norm of the residual = 0.0538), and the resulting parameters are in Table 1. Note that the total efflux terms correspond to the degradation term. We took the value of actin basal concentrations from (*76*), and for Arp2/3 and cofilin, we took the mean of the molarity of the cytoskeleton proteins, hence $(\beta^*, A^*, C^*) = (3,000, 20, 40)$μM.

We use a simplified version of our model that neglects the spatial component (i.e., setting $\rho = 0$ in Eqs. 1 , 7, and 8) to compare the trends (Fig. S11C). Note that the evolution of the normalized concentration of barbed ends in the model is similar to the normalized concentration of β-actin from the experimental data, despite the differences in the evolution of the concentrations of Arp2/3 and cofilin (Fig. S11D). This discrepancy between the evolution in the experimental data and the model arises because the nucleation and severing events in the model reduce the protein concentrations (terms $-f_{nuc}$ and $-f_{sev}$ in Eqs. (7) and (8), respectively). During our data fitting, we did not account for the interactions between ABPs and actin because the experimental setup does not distinguish when cofilin is bound or unbound to F-actin (*25*) (Eq. S6). For example, the slow decay of cofilin normalized concentration in the data is attributed to cofilin binding to F-actin and stabilizing it (*25*). However, in the model, cofilin normalized concentration sharply decays after stimulation to a value below pre-stimulation due to enhancement of severing events induced by the increase of F-actin. The concentration of Arp2/3 in the model exhibits a similar decay due to the increase of nucleation events promote by the increase of F-actin. We are interested in the evolution of the spine expansion upon LTP, which we assumed to be regulated by the force generated by actin polymerization. Hence, we considered this model to be a good proxy because it exhibits a trend in the evolution of barbed ends similar to the evolution of β-actin in the experimental data.

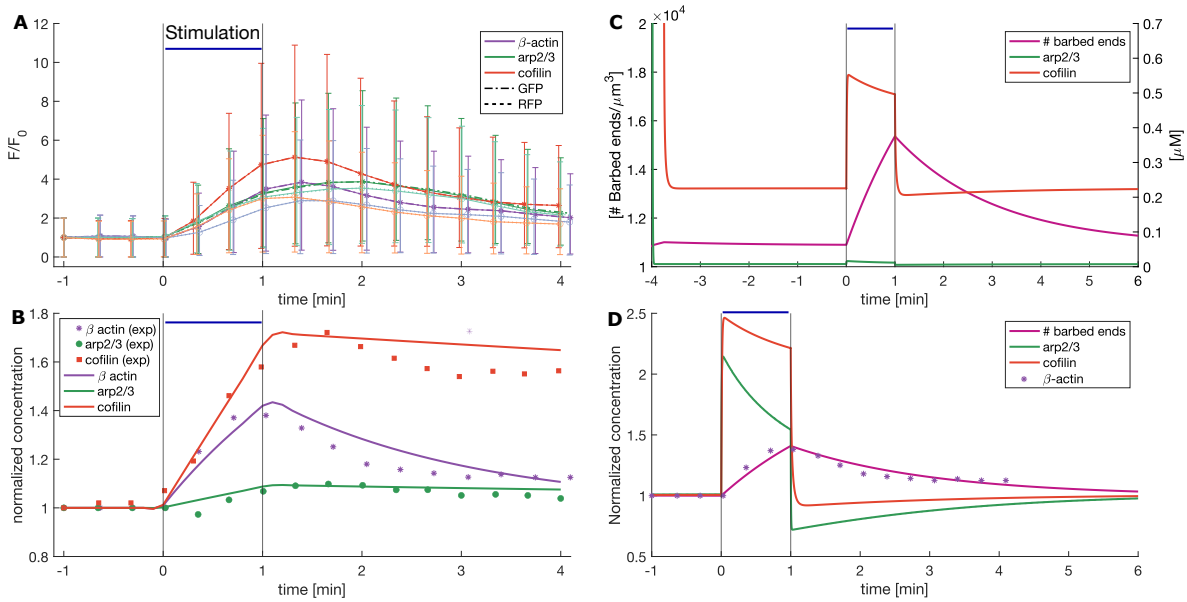

Figure S11: Obtaining model parameters from data. Stimulus is present from $t = 0$ to $t = 1$ minute, indicated by the black vertical lines in the plot. During this time, there is glutamate uncaging and the stimulus-triggered influx $I_S > 0$. **A)** Experimental data taken from (*25*). Asterisks and dots correspond to the mean of the total fluorescence intensity (F) over the averaged baseline fluorescence intensity (F0) of GFP and RFP, which gives a proxy for the amount of proteins in the spine and its volume, respectively. Errors bars denote SEM. **B)** Markers: Normalized concentrations calculated as GFP/RFP from (A). Lines: evolution of the normalized concentration of proteins in the model used to fit the influx, efflux and decaying rate parameters (squared norm of the residual = 0.0538). **C)** Evolution of the non-spatial version of the model in Eqs. (1), (7), and (8). Note that the left y-axis shows the units of barbed ends per μm^3 and the right y-axis the units of Arp2/3 and cofilin concentration. **D)** Normalized change in concentration of the quantities on (C) over time obtained by dividing the variable value over its value before the stimulation. Asterisks correspond to the β-actin data points in (B).

S2.3 Viscoelastic model

We use the same procedure as in S2.2 to fit the volume evolution to a Kelvin-Voigt Model given by:

$$\sigma = R\epsilon + \upsilon \frac{\mathrm{d}\epsilon}{\mathrm{d}t}, \tag{S7}$$

where σ is the stress, ϵ the strain, R the elastic modulus, and υ the coefficient of viscosity. For the fitting, we assume that a constant stress $\sigma_0 = 1$ pN is applied during the stimulation window and set $\sigma_0 = 0$ pN after the stimulus. We take the spine volume as a proxy of the change in length (ϵ). All the fittings where done with the same initial conditions over two minutes, the first one corresponding to the stimulation window. To compare our results with those of experimental data in (*28*), we apply the complex representation to Eq. (S7) as in (*77*), which gives

$$G' = R \quad \text{and} \quad G'' = \upsilon. \tag{S8}$$

S3 Force-velocity calculation

We calculate the force-velocity for spine growth by taking the membrane horizontal displacement at the middle of the spine head and measuring the forces locally. We define the local force to be equal to the average force generated by the nodes of the triangular face that intersects the cell

displacement trajectory. Thus, at the start of the simulation, we select a location in the middle of the spine head and at every time-step, we find the triangle in the mesh that intersects the trajectory of a horizontal line passing through the selected location.

S4 Homogeneous stimulus-triggered influx

We examined whether the spatial distribution of the number of barbed ends and the concentration of Arp2/3 and cofilin settle to a steady state. Note that Figure S12 shows the stabilization process for the case of homogeneous stimulus-triggered influx in Figure 2. We ran the simulation for 1 minute while keeping the membrane fixed, corresponding to Figure S12A. We observed that the barbed ends and ABPs settle to a heterogeneous spatial configuration (Fig. S12E) at the end of 1 minute because the motion of the barbed ends and the bulk flow of Arp2/3 and cofilin reach an equilibrium. Note that the number of barbed ends is greater at locations near the membrane where the curvature of the spine membrane is low due to the motion of the barbed ends toward the membrane (ρ in Eq. 1), which balances the actin polymerization velocity and the retrograde flow (Eq. 2). We allowed membrane evolution for 3 minutes (Eq. 9). We found that the spine settled to a new equilibrium shape in which the length of the neck was reduced and the head size increased. In this new equilibrium, the spatial configuration of the barbed ends and ABPs remains heterogeneous.

Next, we integrated the values of the number of barbed ends and concentration of ABPs over time in the cubic domain. Figure S12F shows that the total values of the number of barbed ends, Arp2/3, and cofilin concentration quickly reach a steady state at the start of the simulation where the spine membrane is fixed. When the membrane evolves, the total value of the variables fluctuates around a steady state, indicating that the system is initialized to a stable steady state. Note that there is a small increase in the spine volume and surface area when we allowed membrane changes (after minute 1), but they rapidly settle to a stable value prior to the stimulus (Fig. S12G). The spine volume and the surface area increase rapidly during the stimulus and settle to a new higher steady state value after the stimulus is turned off. We also measured the radius of the spine neck and head at the same height over time ($z \sim 0.47$ µm and $z = 0.84$µm, respectively, see Fig. S12H). While the spine head radius shows a similar trend to the spine volume and surface area, the spine neck increases upon LTP induction and keeps rising after the stimulus finishes until it reaches a new steady state, consistent with (*12*). After normalizing the values of volume, surface area, spine neck radius, and head radius (Fig. S12J), we observed a large increase in the spine volume (45.29%) and a small increase in the spine surface area (10.88%) and spine head radius (14.41%). Although the spine neck radius shows a small increase (14.15%) during the stimulus window, it enlarges by 33.81% at the end of the simulation. Figure S12I shows the normalized variables of Figure S12F divided over the normalized volume. The final spine shape is shown in Figure S12C. Note that the homogeneous stimulus-triggered influx model also fit well a viscoelastic model (Fig. S12D).

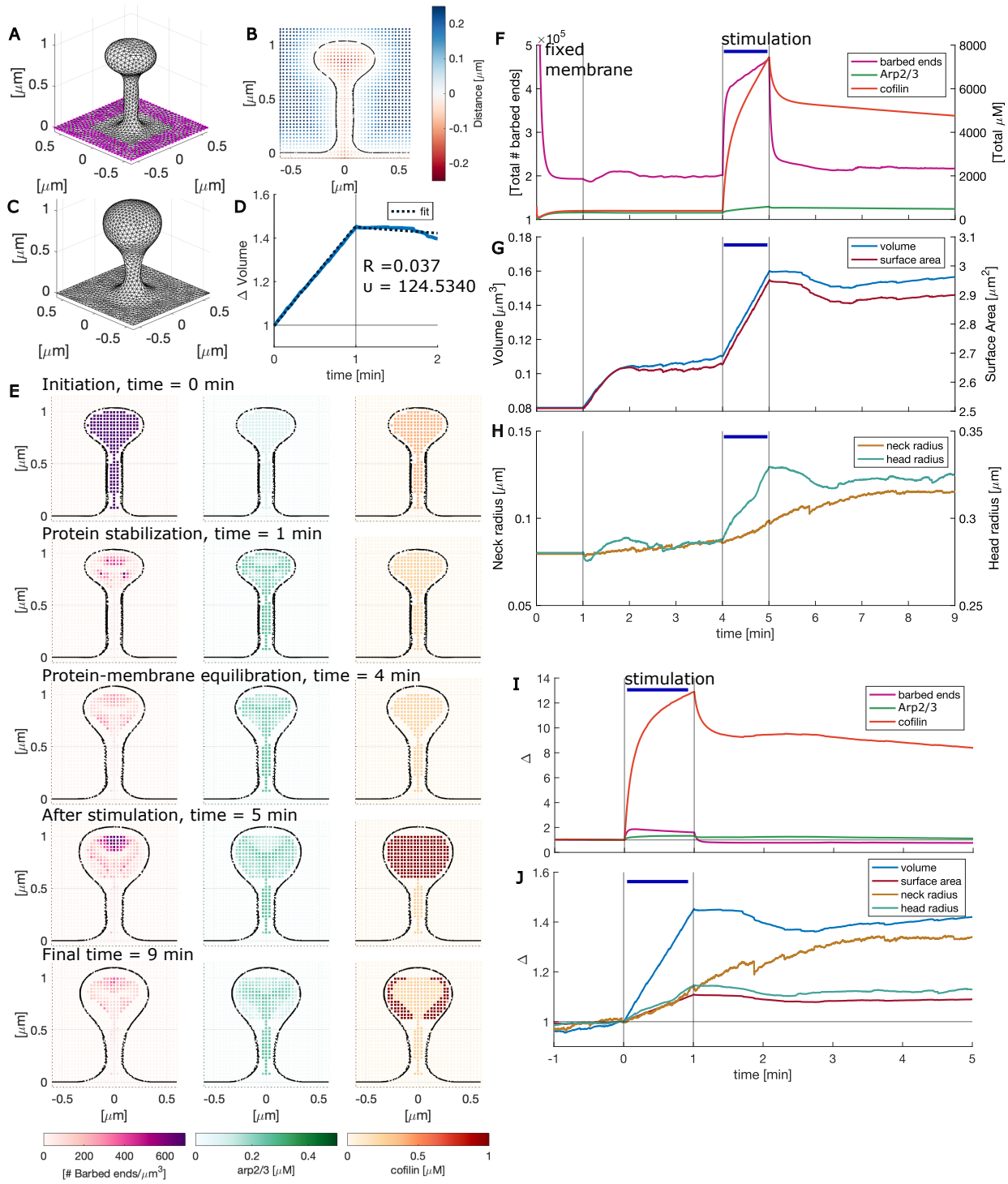

Figure S12: Protein temporal and spatial evolution upon LTP. **A)** Initial configuration of the dendritic spine. Magenta dots correspond to the vertices of the dendritic shaft that remain fixed throughout the simulation. **B)** Slide of a dendritic spine at $x = 0$ μm showing the value of the signed distance function in the cubic domain $\mathcal{L}$. **C)** Dendritic spine at the end of the simulation. **D)** Fit of the normalized volume trace to a viscoelastic model (squared norm of the residual = 0.0859). **E)** Snapshots of the dendritic spine slide at $x = 0$μm showing the number of barbed ends per micron and the Arp2/3 and cofilin concentration at different times. See movie S1. **F)** Sum of the value of the number of barbed ends per micron, and Arp2/3 and cofilin concentration in the cubic domain. Vertical black lines signal the times when the simulation changes: at the start, the membrane is fixed, then the membrane is allowed to move until the simulation stabilizes before the stimulus is given (horizontal blue line). **G)** Spine volume and surface area evolution over time. **H)** Spine head and neck radius evolution over time. **I)** Normalized (to $t = 0$ min) change in the number of barbed ends and concentration of Arp2/3 and cofilin in the spine (concentration/volume). **J)** Normalized (to $t = 0$ min) volume, surface area, spine neck, and head radius.

To further inspect how the forces generated by the membrane and actin polymerization influence the shape evolution of the spine, we plotted the membrane mesh color-coded by the norm of these forces (Fig. S13A). During the first phase of the simulation, where the membrane is fixed, we observed that the actin polymerization force dominates in the spine head while the membrane force dominates in the spine neck. When the membrane was allowed to move, both forces decayed, showing that the spine settled to a minimum mechanical energy state.

To quantify the evolution of the forces generated by the membrane and actin polymerization over time, we integrated the norm of the force vectors corresponding to each node of the spine membrane (Fig. S13B). At the start of the simulation, where the spine membrane is fixed, there is a rapid decay of the total force generated by actin polymerization corresponding to the decay in the number of barbed ends (Fig. S12F). The forces settled to a stable value when the membrane is allowed to evolve. The normalized forces are shown in Figure S13C. The force-velocity relationships are shown in Figures S13D-F, for the forces generated by the membrane, actin polymerization, and both, respectively.

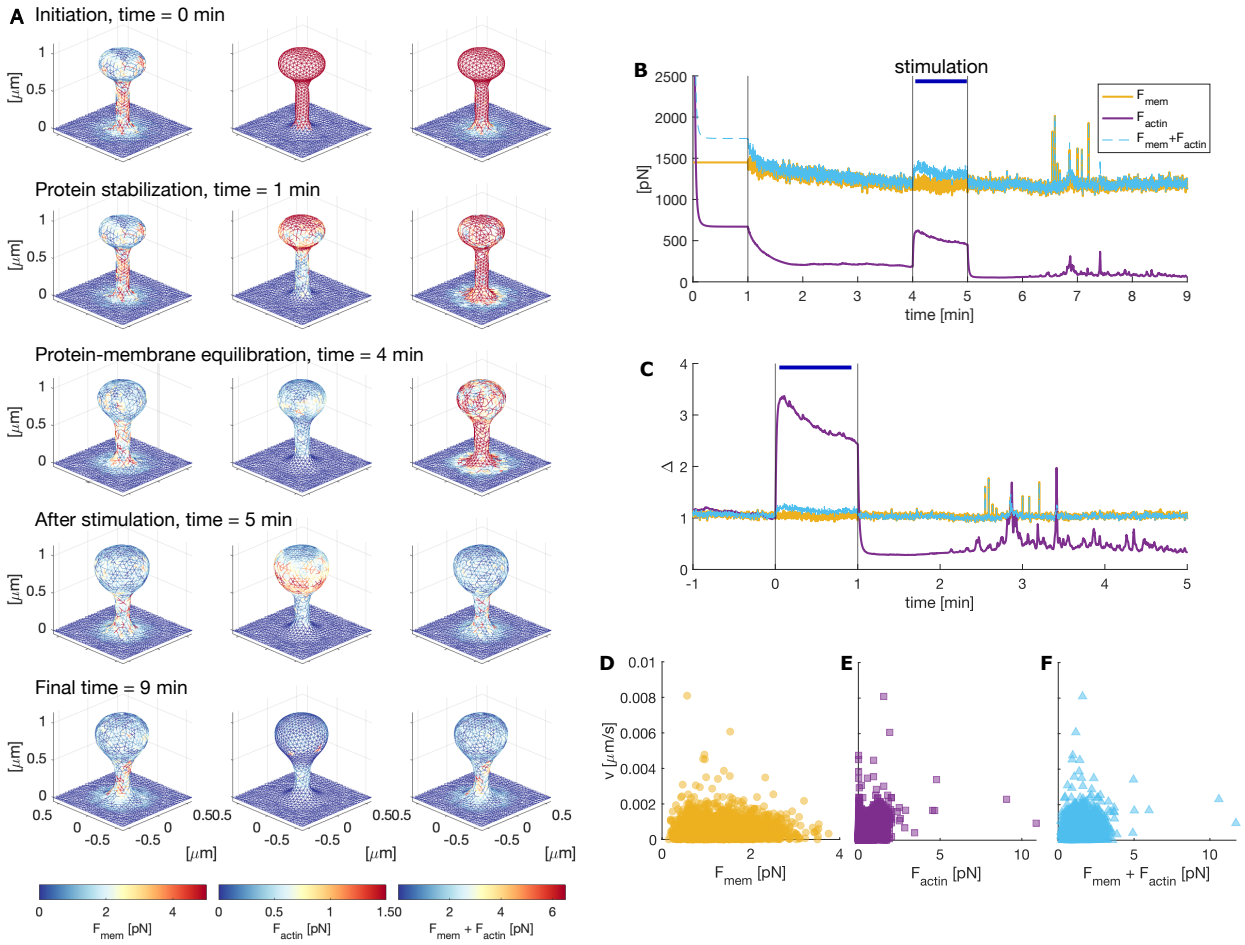

Figure S13: Quantification of spine evolution over time. **A)** Temporal evolution of the forces generated by the membrane, and actin polymerization, or both, color-coded for the norm of the force vectors. **B)** Sum of the norm of the forces $F = ||\mathbf{F}||$ generated by the membrane and actin polymerization over the mesh vertices. **C)** Normalized (to $t = 0$ min) total force F. **D-F)** Plot of the protrusion velocity over force generated by the membrane, actin polymerization, and both, respectively. The protrusion velocity was calculated as the horizontal displacement of the membrane at the middle of the spine head. The force was taken locally, i.e., the force corresponding to the triangular face that intersects the displacement vector.

S5 Actin-generation built in redundancy

The Ca^{2+} entry due to the spine activation of the NMDARs triggers a signalling cascade that leads to activation of Arp2/3 and cofilin (*24*) (Fig. 1C). Thus, we investigated whether such activation enhances the spine enlargement. For this, we assumed that the activated proteins contribute to the proteins entering upon LTP induction. Thus, we increased the value of $I_{S,A}$ and $I_{S,C}$ by 50%. We found that the increase of Arp2/3 and cofilin (Fig. S14C-D) had no effect on the production of barbed ends (Fig. S14B). Moreover, there is a slight reduction in the peak of the normalized volume, form 1.4495 to 1.4268 μm^3 (Fig. S14A). Thus, we concluded that the effect of the increase in Arp2/3 and cofilin in the volume is minimal.

We then examined the effect of disrupting the stimulus-triggered influx of barbed ends, Arp2/3, and cofilin in spine enlargement. We observed that setting $I_{S,A} = 0$ or $I_{S,C} = 0$ during stimulation had an insignificant effect on spine enlargement: the normalized increase in volume at the end of the stimulation changes from 1.4495 to 1.4104 and 1.4288, respectively (Fig. S14A). Only impeding the stimulus-triggered influx of actin hindered the increase in spine volume to only 5% after stimulation. Note that when $I_{S,\beta} = 0$, the peak of normalized Arp2/3 and cofilin concentration after stimulation exhibits an approximately three-fold increase, proving that these proteins are sequestrated by the stimulus-triggered influx of actin through nucleation and severing events (Fig. S14C-D). The results suggest that spine volume increase is highly insensitive to Arp2/3 or cofilin deprivation. We inferred that the enhancement of barbed ends after LTP induction is sufficient to overcome the membrane force and allow spine enlargement, in line with previous theoretical work in cell protrusion (*36*, *53*).

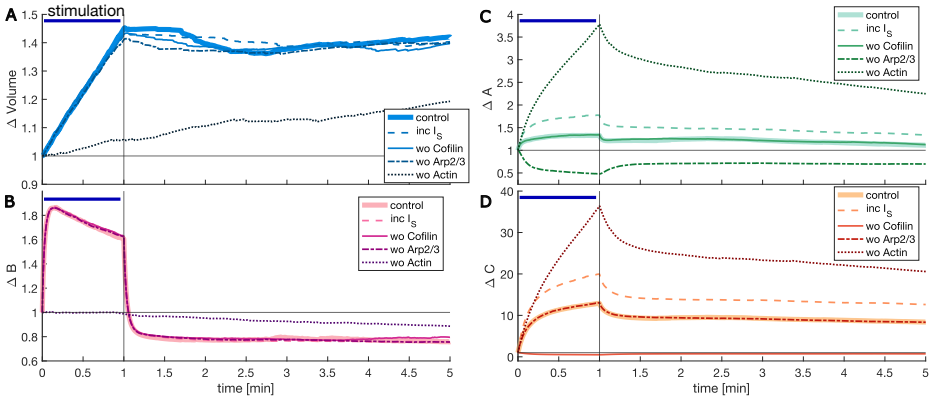

Figure S14: Influence of barbed ends, Arp2/3, and cofilin in spine volume. **A)** Normalized spine volume for different set ups where either the influx of Arp2/3, cofilin or actin are excluded, or the influx of Arp2/3 and cofilin are enhaced 50%. Vertical black line signals the end of the stimulus window. **B-D)** Evolution of normalized number of barbed ends per micron, apr2/3 and cofilin concentration over time.

S6 Membrane bending stiffness dictates spine morphology

The bending stiffness of neuronal membranes varies depending on the neuron type and compartment (i.e., cell body, neurite, growth cone) from 1.8×10^{-19} to 2.3×10^{-19} J (*50*). In our model, we noticed that the total membrane force did not increase during the stimulation window (Fig. S13C). However, the total membrane force diminished the increase of the force generated by actin polymerization. Therefore, we further investigated the effect of the force generated by the membrane on spine growth upon stimulation. For this, we varied the bending stiffness κ by 25% its value in the simulations. We observed a change in the spine shape after stimulation and at the end of the

simulation. When increasing membrane stiffness, the spines show a wider head and thinner neck (Fig. S15A). Decreasing the bending stiffness results in spines with a thinner head and wider neck (Fig. S15B). Note that the thinner the neck, the larger force generated by the membrane.

Interestingly, we observed that the volume of the spine remains constant after stimulation when increasing κ, hinting at the function of membrane stiffness in maintaining the spine shape (Fig. S15C). However, the maximum change in volume is similar for the different values of bending stiffness ($V =$ 1,4495, 1.4580, and 1.4287 μm^3 for κ, 1.25κ, and 0.75κ, respectively). The most notable change in the normalized number of barbed ends, Arp2/3, and cofilin for different values of κ occurs after the stimulation window (Figs. S15D-F). The normalized concentrations of B, A, and C are smaller for increased bending stiffness. We found that these lower values result in less fluctuation of the forces (Figs. S15G-I). Although the changes of the force generated by the membrane (Fig. S15G) and the force generated by actin polymerization (Fig. S15H) are similar for the different values of κ, the sum of these forces show different behaviour (Fig. S15I). A decrease in κ results on a increase of the overall force (i.e., $||\mathbf{F}_{mem}+\mathbf{F}_{actin}||$) because the force generated by the membrane is not enough to counteract the force generated by actin locally. Taken all together, we conclude that the resistance offered by the membrane affects the spine shape dynamics.

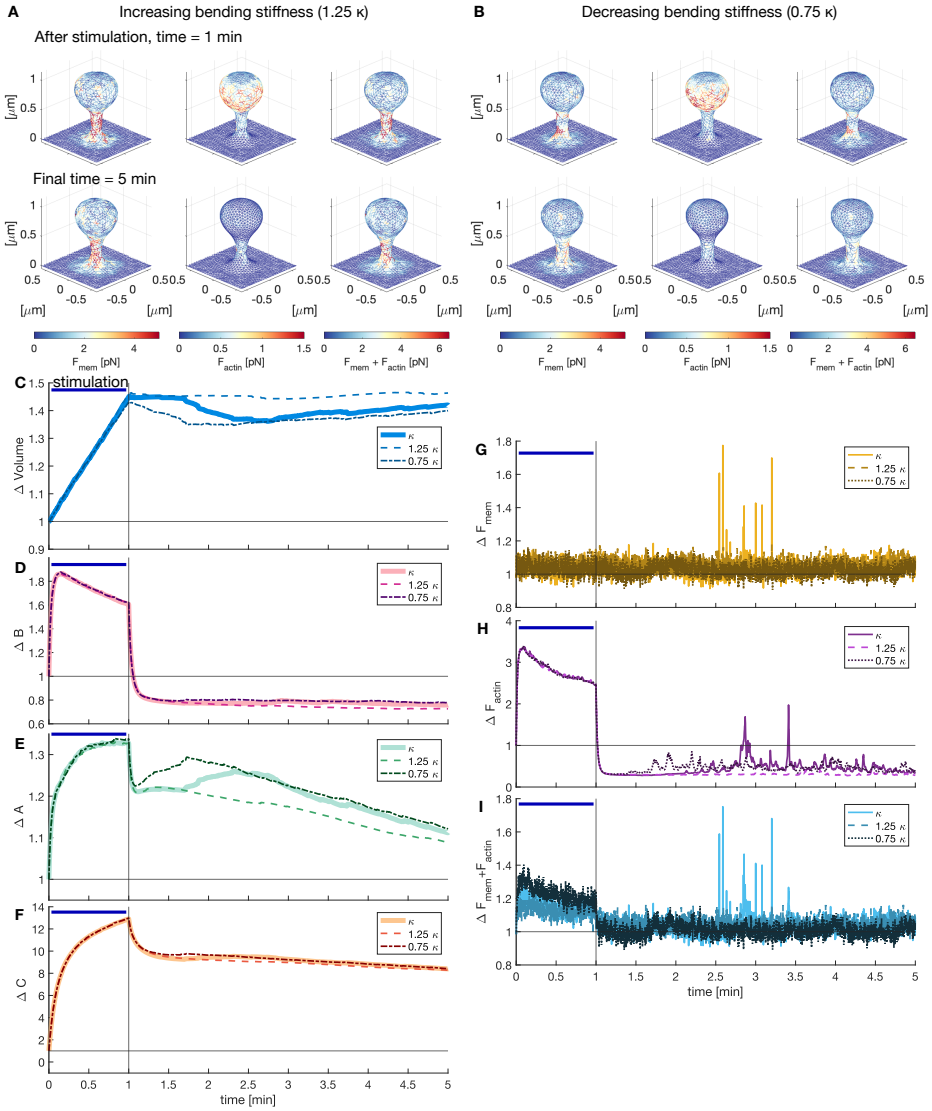

Figure S15: Effect of membrane bending stiffness on dendritic spine expansion. **A)** Dendritic spines after stimulation (top) and at the end of the simulation (bottom), color-coded for the norm of the force vector $F = ||\mathbf{F}||$ at each node of the membrane mesh. The membrane stiffness κ was increased by 25% its value. **B)** Same as (A) but decreasing the value of the membrane stiffness to 75% its value. **C)** Normalized (to $t = 0$ min) volume for different values of κ over time. **D-F)** Normalized (to $t = 0$ min) number of barbed ends, concentration of Arp2/3 and cofilin in the spine for different values of κ over time. **G-I)** Normalized (to $t = 0$ min) total force F generated by the membrane, actin polymerization, and both, for different values of κ over time.

References

1. K. M. Harris, *Current Opinion in Neurobiology*, Cellular Neuroscience **63**, 189–197, ISSN: 0959-4388, DOI `10.1016/j.conb.2020.04.009` (Aug. 1, 2020).
2. Y. Nakahata, R. Yasuda, *Frontiers in Synaptic Neuroscience* **0**, ISSN: 1663-3563, DOI `10.3389/fnsyn.2018.00029` (2018).
3. S. Okabe, *Molecular and Cellular Neuroscience* **109**, 103564, ISSN: 1044-7431, DOI `10.1016/j.mcn.2020.103564` (Dec. 1, 2020).

4. M. Matsuzaki, N. Honkura, G. C. R. Ellis-Davies, H. Kasai, *Nature* **429**, 761–766, ISSN: 1476-4687, DOI 10.1038/nature02617 (June 2004).

5. K.-I. Okamoto, T. Nagai, A. Miyawaki, Y. Hayashi, *Nature Neuroscience* **7**, 1104–1112, ISSN: 1546-1726, DOI 10.1038/nn1311 (Oct. 2004).

6. H. Kasai, M. Fukuda, S. Watanabe, A. Hayashi-Takagi, J. Noguchi, *Trends in Neurosciences* **33**, 121–129, ISSN: 0166-2236, DOI 10.1016/j.tins.2010.01.001 (Mar. 1, 2010).

7. R. Yuste, T. Bonhoeffer, *Annual review of neuroscience* **24**, 1071–1089, ISSN: 1545-4126, DOI 10.1146/annurev.neuro.24.1.1071 (Jan. 1, 2001).

8. T. V. P. Bliss, T. Lømo, *The Journal of Physiology* **232**, 331–356, ISSN: 1469-7793, DOI 10.1113/jphysiol.1973.sp010273 (1973).

9. M. F. Bear, R. C. Malenka, *Current Opinion in Neurobiology* **4**, 389–399, ISSN: 0959-4388, DOI 10.1016/0959-4388(94)90101-5 (June 1, 1994).

10. S.-H. Shi *et al.*, *Science* **284**, 1811–1816, DOI 10.1126/science.284.5421.1811 (June 11, 1999).

11. K. M. Harris, J. K. Stevens, *Journal of Neuroscience* **9**, 2982–2997, ISSN: 0270-6474, 1529-2401, DOI 10.1523/JNEUROSCI.09-08-02982.1989 (Aug. 1, 1989).

12. J. Tønnesen, G. Katona, B. Rózsa, U. V. Nägerl, *Nature Neuroscience* **17**, 678–685, ISSN: 1546-1726, DOI 10.1038/nn.3682 (May 2014).

13. J.-Y. Chang *et al.*, *Neuron* **94**, 800–808.e4, ISSN: 0896-6273, DOI 10.1016/j.neuron.2017.04.041 (May 17, 2017).

14. A. Matus, M. Ackermann, G. Pehling, H. R. Byers, K. Fujiwara, *Proceedings of the National Academy of Sciences* **79**, 7590–7594, DOI 10.1073/pnas.79.23.7590 (Dec. 1982).

15. L. A. Cingolani, Y. Goda, *Nature Reviews Neuroscience* **9**, 344–356, ISSN: 1471-0048, DOI 10.1038/nrn2373 (May 2008).

16. N. Honkura, M. Matsuzaki, J. Noguchi, G. C. R. Ellis-Davies, H. Kasai, *Neuron* **57**, 719–729, ISSN: 0896-6273, DOI 10.1016/j.neuron.2008.01.013 (Mar. 13, 2008).

17. Y. Yang, J.-J. Liu, *Current Opinion in Neurobiology* **74**, 102534, ISSN: 0959-4388, DOI 10.1016/j.conb.2022.102534 (June 1, 2022).

18. T. D. Pollard, G. G. Borisy, *Cell* **112**, 453–465, ISSN: 0092-8674, DOI 10.1016/S0092-8674(03)00120-X (Feb. 21, 2003).

19. D. A. Fortin, T. Srivastava, T. R. Soderling, *The Neuroscientist* **18**, 326–341, ISSN: 1073-8584, DOI 10.1177/1073858411407206 (Aug. 1, 2012).

20. T. D. Pollard, L. Blanchoin, R. D. Mullins, *Annual Review of Biophysics and Biomolecular Structure* **29**, 545–576, DOI 10.1146/annurev.biophys.29.1.545 (2000).

21. I. H. Kim *et al.*, *The Journal of neuroscience* **33**, 6081–6092, ISSN: 1529-2401, DOI 10.1523/jneurosci.0035-13.2013 (Apr. 1, 2013).

22. M. B. Rust *et al.*, *The EMBO Journal* **29**, 1889–1902, ISSN: 0261-4189, DOI 10.1038/emboj.2010.72 (June 2, 2010).

23. E. Andrianantoandro, T. D. Pollard, *Molecular Cell* **24**, 13–23, ISSN: 1097-2765, DOI 10.1016/j.molcel.2006.08.006 (Oct. 6, 2006).

24. P. Rangamani, M. G. Levy, S. Khan, G. Oster, *Proceedings of the National Academy of Sciences* **113**, E5298–E5307, ISSN: 0027-8424, 1091-6490, DOI 10.1073/pnas.1610391113 (Sept. 6, 2016).

25. M. Bosch *et al.*, *Neuron* **82**, 444–459, ISSN: 0896-6273, DOI 10.1016/j.neuron.2014.03.021 (Apr. 16, 2014).

26. R. L. Redondo, R. G. M. Morris, *Nature Reviews Neuroscience* **12**, 17–30, ISSN: 1471-0048, DOI 10.1038/nrn2963 (Jan. 2011).

27. K. Okuda, K. Højgaard, L. Privitera, G. Bayraktar, T. Takeuchi, *European Journal of Neuroscience* **n/a**, ISSN: 1460-9568, DOI 10.1111/ejn.14902.

28. B. A. Smith, H. Roy, P. De Koninck, P. Grütter, Y. De Koninck, *Biophysical Journal* **92**, 1419–1430, ISSN: 0006-3495, DOI 10.1529/biophysj.106.092361 (Feb. 15, 2007).

29. R. F. Kastian *et al.*, *Cell Reports* **35**, 109130, ISSN: 2211-1247, DOI 10.1016/j.celrep.2021.109130 (May 18, 2021).

30. A. Mogilner, L. Edelstein-Keshet, *Biophysical Journal* **83**, 1237–1258, ISSN: 0006-3495, DOI 10.1016/S0006-3495(02)73897-6 (Sept. 1, 2002).

31. N. Tania, E. Prosk, J. Condeelis, L. Edelstein-Keshet, *Biophysical Journal* **100**, 1883–1892, ISSN: 0006-3495, DOI 10.1016/j.bpj.2011.02.036 (Apr. 20, 2011).

32. N. Tania, J. Condeelis, L. Edelstein-Keshet, *Biophysical Journal* **105**, 1946–1955, ISSN: 0006-3495, DOI 10.1016/j.bpj.2013.09.013 (Nov. 5, 2013).

33. Y. Xiong *et al.*, *Biophysical Journal* **98**, 2136–2146, ISSN: 0006-3495, DOI 10.1016/j.bpj.2010.01.059 (May 19, 2010).

34. A. Mogilner, G. Oster, *Biophysical Journal* **71**, 3030–3045, ISSN: 0006-3495, DOI 10.1016/S0006-3495(96)79496-1 (Dec. 1, 1996).

35. K. Doubrovinski, K. Kruse, *Physical Review Letters* **107**, 258103, DOI 10.1103/PhysRevLett.107.258103 (Dec. 16, 2011).

36. C. I. Lacayo *et al.*, *PLOS Biology* **5**, e233, ISSN: 1545-7885, DOI 10.1371/journal.pbio.0050233 (Aug. 28, 2007).

37. I. J. Cajigas *et al.*, *Neuron* **74**, 453–466, ISSN: 0896-6273, DOI 10.1016/j.neuron.2012.02.036 (May 10, 2012).

38. D. M. Tiruchinapalli *et al.*, *Journal of Neuroscience* **23**, 3251–3261, ISSN: 0270-6474, 1529-2401, DOI 10.1523/JNEUROSCI.23-08-03251.2003 (Apr. 15, 2003).

39. A. E. Carlsson, M. A. Wear, J. A. Cooper, *Biophysical Journal* **86**, 1074–1081, ISSN: 0006-3495, DOI 10.1016/S0006-3495(04)74182-X (Feb. 1, 2004).

40. V. I. Risca *et al.*, *Proceedings of the National Academy of Sciences* **109**, 2913–2918, ISSN: 0027-8424, 1091-6490, DOI 10.1073/pnas.1114292109 (Feb. 21, 2012).

41. E. M. De La Cruz, *Journal of Molecular Biology* **346**, 557–564, ISSN: 0022-2836, DOI 10.1016/j.jmb.2004.11.065 (Feb. 18, 2005).

42. W. Helfrich, *Zeitschrift für Naturforschung C* **28**, 693–703, ISSN: 1865-7125, DOI 10.1515/znc-1973-11-1209 (Dec. 1, 1973).

43. H. Krüger, *Computer Simulation Study of Collective Phenomena in Dense Suspensions of Red Blood Cells under Shear* (Springer Science & Business Media, July 18, 2012), 169 pp., ISBN: 978-3-8348-2375-5.

44. M. Deserno, *Chemistry and Physics of Lipids*, Membrane mechanochemistry: From the molecular to the cellular scale **185**, 11–45, ISSN: 0009-3084, DOI 10.1016/j.chemphyslip.2014.05.001 (Jan. 1, 2015).

45. *MATLAB*, version 9.10.0.1710957 (R2021a) Update 4, Natick, Massachusetts, 2021.

46. C. Helf, *MATLAB Isotropic Remesher*, Aug. 5, 2021.

47. *OpenMesh*, version 8.1, 2020.

48. J. Roland, J. Berro, A. Michelot, L. Blanchoin, J.-L. Martiel, *Biophysical Journal* **94**, 2082–2094, ISSN: 0006-3495, DOI 10.1529/biophysj.107.121988 (Mar. 15, 2008).

49. N. A. Frost, H. Shroff, H. Kong, E. Betzig, T. A. Blanpied, *Neuron* **67**, 86–99, ISSN: 0896-6273, DOI 10.1016/j.neuron.2010.05.026 (July 15, 2010).

50. B. Pontes *et al.*, *PLOS ONE* **8**, e67708, ISSN: 1932-6203, DOI 10.1371/journal.pone.0067708 (July 3, 2013).

51. M. Akamatsu *et al.*, *eLife* **9**, ed. by P. Bassereau, V. Malhotra, P. Bassereau, A. Mogilner, e49840, ISSN: 2050-084X, DOI 10.7554/eLife.49840 (Jan. 17, 2020).

52. P. Rangamani, G. Y. Xiong, R. Iyengar, *Progress in Molecular Biology and Translational Science* **123**, 143–167, ISSN: 1878-0814, DOI 10.1016/B978-0-12-397897-4.00002-4 (2014).

53. P. Rangamani *et al.*, *Biophysical Journal* **100**, 845–857, ISSN: 0006-3495, DOI 10.1016/j.bpj.2010.12.3732 (Feb. 16, 2011).

54. J. L. McGrath *et al.*, *Current Biology* **13**, 329–332, ISSN: 0960-9822, DOI 10.1016/S0960-9822(03)00051-4 (Feb. 18, 2003).

55. C. Brangbour *et al.*, *PLOS Biology* **9**, e1000613, ISSN: 1545-7885, DOI 10.1371/journal.pbio.1000613 (Apr. 26, 2011).

56. Y. Y. Huang, E. R. Kandel, *Learning & Memory* **1**, 74–82, ISSN: 1072-0502, 1549-5485, DOI 10.1101/lm.1.1.74 (May 1, 1994).

57. A. F. Hobbiss, Y. Ramiro-Cortés, I. Israely, *iScience* **8**, 161–174, ISSN: 2589-0042, DOI 10.1016/j.isci.2018.09.015 (Oct. 26, 2018).

58. S. S. Suratkal, Y.-H. Yen, J. Nishiyama, *Current Opinion in Neurobiology*, Neurobiology of Learning and Plasticity **67**, 66–74, ISSN: 0959-4388, DOI 10.1016/j.conb.2020.08.006 (Apr. 1, 2021).

59. D. Pantaloni, C. L. Clainche, M.-F. Carlier, *Science* **292**, Publisher: American Association for the Advancement of Science, 1502–1506, DOI 10.1126/science.1059975 (May 25, 2001).

60. I. H. Kim *et al.*, *Nature Neuroscience* **18**, 883–891, ISSN: 1546-1726, DOI 10.1038/nn.4015 (June 2015).

61. Y. Ben Zablah, N. Merovitch, Z. Jia, *Frontiers in Cell and Developmental Biology* **8**, ISSN: 2296-634X (2020).

62. J. Bär, O. Kobler, B. van Bommel, M. Mikhaylova, *Scientific Reports* **6**, 37136, ISSN: 2045-2322, DOI 10.1038/srep37136 (Nov. 14, 2016).

63. H. Alimohamadi, M. K. Bell, S. Halpain, P. Rangamani, *Frontiers in Physiology* **12**, 836, ISSN: 1664-042X, DOI 10.3389/fphys.2021.657074 (2021).

64. G. G. Turrigiano, *Cell* **135**, 422–435, ISSN: 0092-8674, DOI 10.1016/j.cell.2008.10.008 (Oct. 31, 2008).

65. D. Ohadi *et al.*, *Biophysical Journal* **117**, 1963–1980, ISSN: 0006-3495, DOI 10.1016/j.bpj.2019.10.003 (Nov. 19, 2019).

66. M. Bell, T. Bartol, T. Sejnowski, P. Rangamani, *The Journal of General Physiology* **151**, 1017–1034, ISSN: 1540-7748, DOI 10.1085/jgp.201812261 (Aug. 5, 2019).

67. M. K. Bell, M. V. Holst, C. T. Lee, P. Rangamani, en, *J. Gen. Physiol.*, 2021.05.06.442994 (Aug. 2022).

68. D. Ohadi, P. Rangamani, *Biophysical Journal* **117**, 1981–1994, ISSN: 0006-3495, DOI 10.1016/j.bpj.2019.10.004 (Nov. 19, 2019).

69. M. K. Bell, C. T. Lee, P. Rangamani, en, *J. Physiol.* (Nov. 2022).

70. S. Čanić, *Bulletin of the American Mathematical Society* **58**, 79–106, ISSN: 0273-0979, 1088-9485, DOI 10.1090/bull/1703 (Jan. 2021).

71. Z. Peng *et al.*, *Proceedings of the National Academy of Sciences* **110**, 13356–13361, ISSN: 0027-8424, 1091-6490, DOI 10.1073/pnas.1311827110 (Aug. 13, 2013).

72. M. Bonilla-Quintana, F. Wörgötter, *Scientific Reports* **11**, 7072, ISSN: 2045-2322, DOI 10.1038/s41598-021-86367-z (Mar. 29, 2021).

73. M. Bonilla-Quintana, F. Wörgötter, C. Tetzlaff, M. Fauth, *Frontiers in Synaptic Neuroscience* **0**, ISSN: 1663-3563, DOI 10.3389/fnsyn.2020.00009 (2020).

74. J. Schindelin *et al.*, *Nature Methods* **9**, 676–682, ISSN: 1548-7105, DOI 10.1038/nmeth.2019 (July 2012).

75. D. R. Muir, B. Kampa, *Frontiers in Neuroinformatics* **0**, ISSN: 1662-5196, DOI 10.3389/fninf.2014.00085 (2015).

76. M. S. Helm *et al.*, *Nature Neuroscience* **24**, 1151–1162, ISSN: 1546-1726, DOI 10.1038/s41593-021-00874-w (Aug. 2021).

77. Y. C. Fung, *Biomechanics: Mechanical Properties of Living Tissues* (Springer Science & Business Media, Mar. 14, 2013), 585 pp., ISBN: 978-1-4757-2257-4.